Numerical predictions of vibration responses and flow energy conversion efficiency of side-by-side cylinders at moderate Reynolds number

by Kylie Hirth

Submission date: 09-Aug-2024 02:04AM (UTC-0500)
Submission ID: 2429426778
File name: ciency_of_side-by-side_cylinders_at_moderate_Reynolds_number.pdf (1.97M)
Word count: 13068
Character count: 66218

Applied Ocean Research 129 (2022) 103392

Contents lists available at ScienceDirect

Applied Ocean Research

journal homepage: www.elsevier.com/locate/apor

Numerical predictions of vibration responses and flow energy conversion efficiency of side-by-side cylinders at moderate Reynolds number

Yosua Heru Irawan [a], Syed Ahmad Raza [b], Ming-Jyh Chern [a,*]

[a] Department of Mechanical Engineering, National Taiwan University of Science and Technology, Taipei 106335, Taiwan
[b] Department of Mechanical Engineering, NED University of Engineering & Technology, Karachi 124087, Pakistan

ARTICLE INFO

Keywords:
Vortex-induced vibration
Lock-in
Side-by-side cylinders
Large eddy simulation
Flow energy converter
Clean energy

ABSTRACT

Vortex-induced vibration (VIV) of two circular cylinders in a side-by-side (SBS) configuration was modelled using three-dimensional numerical simulation at Reynolds number Re = 1,000. The VIV parameter values used for the study were mass ratio, $m^* = 10.0$, damping ratio, $\zeta = 0.01$, and a range of reduced velocities, $U_R^* = 2.0$ to 10.0. Various VIV responses were investigated, such as amplitude, frequency, and response correlation for gap ratios $1.0 \leqslant g^* \leqslant 3.0$. Moreover, the efficiency of flow energy conversion was determined to assess the potential of this configuration for VIVACE (Vortex-Induced Vibration Aquatic Clean Energy). For comparison, the VIV responses and efficiency of the single-cylinder case were also presented with identical variables. It was found that the optimal gap ratio between the SBS cylinders was in the interval of $1.0 \leqslant g^* \leqslant 1.2$. A significant increase in efficiency occurred in the initial excitation region between $4.0 \leqslant U_R^* \leqslant 5.0$. Above this range, the efficiency was less than that of a single cylinder. In the case of SBS cylinders, the soft lock-in appeared to start early. The anti-phase correlation led to a significant increase in the vibration response as well as efficiency. The increase in maximum efficiency was more than twofold.

1. Introduction

A circular cylinder is one of the simple geometries that is often used to simplify various engineering structures such as cooling towers, chimneys, and riser pipes. Any fluid–structure interaction (FSI) problem is a complex issue that arises and must be solved if the involved structures interact with fluid flow. The interaction between fluid flow and a rigid cylinder can be represented by the case of flow past a circular cylinder. In this case, the vortex-shedding phenomenon will begin to appear when the Reynolds number Re > 40. The Reynolds number is defined as $\mathrm{Re} = U_\infty D/\nu$, where U_∞ is the upstream uniform velocity, D is the diameter of the circular cylinder, and ν is the kinematic viscosity of the fluid. When the circular cylinder structure is enabled to move in the cross-flow direction, a one-degree of freedom (1-DOF) vortex-induced vibration (VIV) phenomenon will occur. Vibrations with a relatively large amplitude will occur when the frequency of the vortex-shedding approaches the natural frequency of the vibrating cylinder in quiescent water. This phenomenon is also known as the synchronization phenomenon. Almost all engineering structures interacting with fluid flow are designed to avoid this phenomenon because large vibration amplitudes can damage or destroy the structure.

Many experimental studies have investigated the VIV of an elastically mounted circular cylinder with 1-DOF motion. Several VIV measurements from Khalak and Williamson (1996, 1997, 1999) showed that the synchronization phenomenon of the vibrating circular cylinder occurs over a range of reduced velocities. The reduced velocity is expressed as $U_R^* = U_\infty / f_n D$, where f_n represents the natural frequency of the vibrating cylinder in quiescent water. The vortex-shedding frequency was found to be locked onto the vibrating cylinder's frequency. This range is identified as the lock-in region of the VIV phenomenon and is characterized by a constant frequency ratio and high vibration amplitudes. The other VIV parameters are mass ratio (m^*) and damping ratio (ζ), where m^* represents the ratio of the cylinder mass to the displaced fluid mass, and ζ represents the ratio of the actual damping to the critical damping. Govardhan and Williamson (2000) divided the responses of 1-DOF VIV into two types, namely high-($m^*\zeta$) type and low-($m^*\zeta$) type. The high-($m^*\zeta$) consists of the initial excitation branch and lower branch responses. For the low-($m^*\zeta$), a third response appeared, namely the upper branch. In addition, numerical simulation has also been used to investigate the VIV phenomenon of the elastically mounted circular cylinder. Guilmineau and Queutey (2004) used a two-dimensional (2-D) Reynolds-Averaged Navier–Stokes (RANS) simulation to investigate the VIV responses of the elastically mounted circular cylinder. The complete VIV responses from this study were in good agreement with the response from experimental measurements.

* Corresponding author.
E-mail address: mjchern@mail.ntust.edu.tw (M.-J. Chern).

https://doi.org/10.1016/j.apor.2022.103392
Received 20 August 2022; Received in revised form 10 October 2022; Accepted 20 October 2022
Available online 4 November 2022

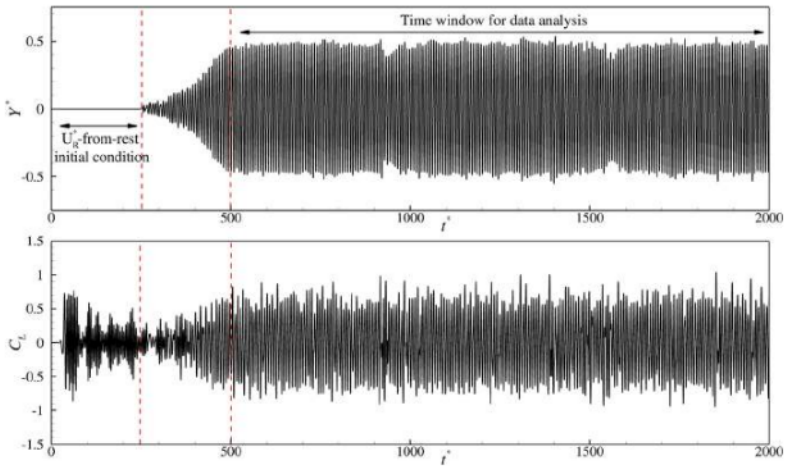

Fig. 1. Time-series data of cylinder displacement and lift coefficient from single-cylinder case at $U_R^* = 7.0$.

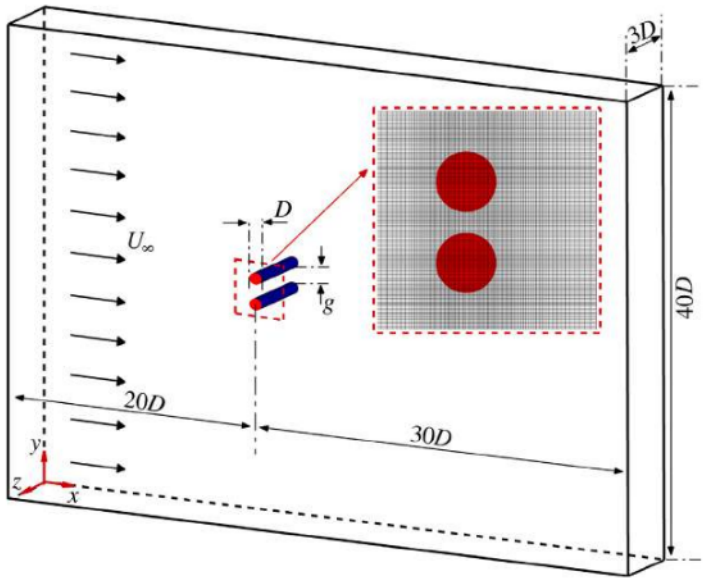

Fig. 2. Computational domain.

However, the upper branch response range was narrower as compared to the experimental data. This result was also confirmed by another numerical study by Pan et al. (2007). Lucor et al. (2005) and Zhao et al. (2014) performed three-dimensional (3-D) Direct Numerical Simulation (DNS) to study the 1-DOF VIV on the elastically mounted circular cylinder. Their findings were also consistent with previously published data. Only the amplitude response in the upper branch was slightly lower than the measurement data from the VIV experiment. More results from experiments and numerical studies of VIV can be found in the following review papers (Sarpkaya, 2004; Williamson and Govardhan, 2004, 2008; Bearman, 2011; Fernandes et al., 2014; Wang et al., 2020; Lv et al., 2021b).

Recently, Bernitsas et al. (2008) succeeded in utilizing VIV for harvesting energy from fluid flow via Vortex-induced Vibration Aquatic clean energy (VIVACE). Unlike the previously mentioned engineering structures, VIVACE is designed to maximize the synchronization phenomenon for utilization as a renewable energy resource. Chang et al. (2011) used Passive Turbulent Control (PTC) to enhance the synchronization range and flow energy conversion of the vibrating cylinder at 30,000 ≤ Re ≤ 120,000. PTC induces higher vorticity and lift force by triggering flow separation and energizing the boundary layer. With the appropriate PTC, flow energy conversion to mechanical energy is significantly improved. Raghavan and Bernitsas (2011) conducted VIVACE experiment at 20,000 ≤ Re ≤ 6.0 x 10^6 and found that the synchronization range increased when Re increased. In order to study the influence of mass ratio, damping and stiffness on the performance of VIVACE converter, Sun et al. (2016) conducted an experiment of flow-induced motions at 30,000 ≤ Re ≤ 120,000. It was found that the VIV synchronization range shifts to higher U_R^* with increased spring stiffness, leading to a lower gap between VIV and galloping. Here, galloping is a flow-induced motion type with lower frequencies and larger amplitudes than VIV, with the amplitude perpendicular to U_R^*. The harnessed power increased with the increase of mass ratio when galloping occurred. Besides VIVACE, another innovation that uses VIV

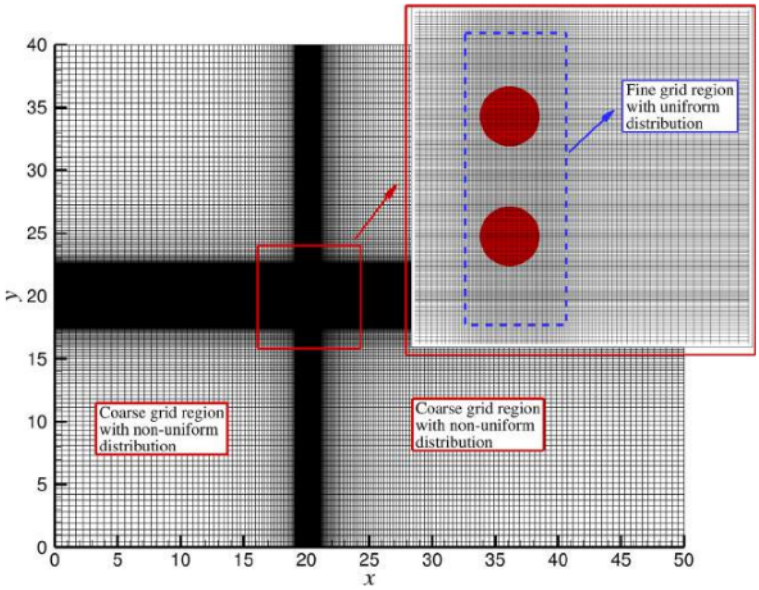

Fig. 3. Complete layout of grid composition at x–y plane.

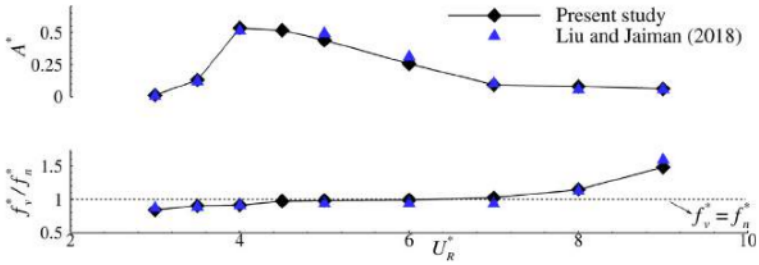

Fig. 4. The validation result of vibration responses (amplitude and frequency ratio) of an upper cylinder in a SBS arrangement.

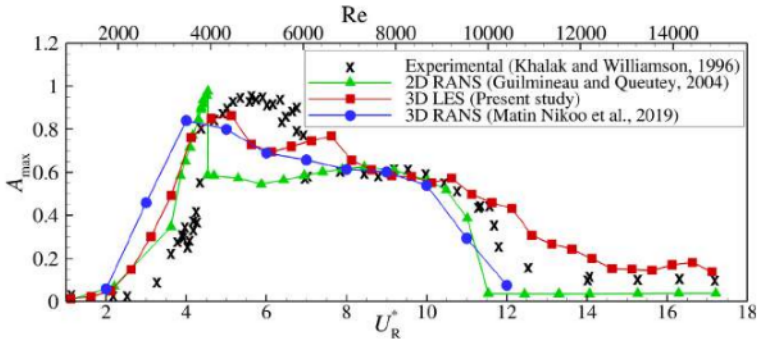

Fig. 5. The vibration response (maximum amplitude) of a single cylinder in the range of Reynolds number.

to harvest energy from fluid flows is the vortex-induced vibration piezoelectric energy harvester (VIVPEH). Recently, Wang et al. (2019) proposed a novel design of a piezoelectric energy harvester that could allow the transition from VIV mode to galloping mode.

Compared with a single-cylinder case, FSI problems become more complex when the fluid flow interacts with multiple circular cylinders. Among the various combinations, the multiple cylinders in a side-by-side (SBS) configuration have become quite popular for investigation. Information on the flow properties formed in the case of flow past SBS cylinders is comprehensively summarized in the following review papers (Sumner, 2010; Zhou and Alam, 2016). The variation of surface-to-surface distance or gap between SBS cylinders produces different wake patterns. A single vortex street appears when the gap between the SBS cylinders is less than $0.2D$. For a larger gap, two cylinders in the SBS position generate separate wakes, which can lead to an in-phase or anti-phase pattern (Carini et al., 2014). Chen et al. (2022a) used

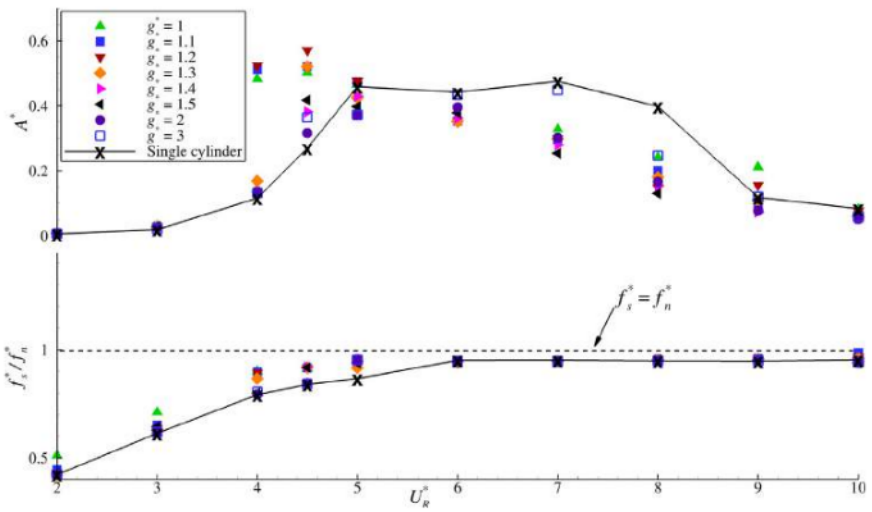

Fig. 6. Amplitude and frequency responses for VIV of two cylinders in an SBS arrangement in the range of U_R^*.

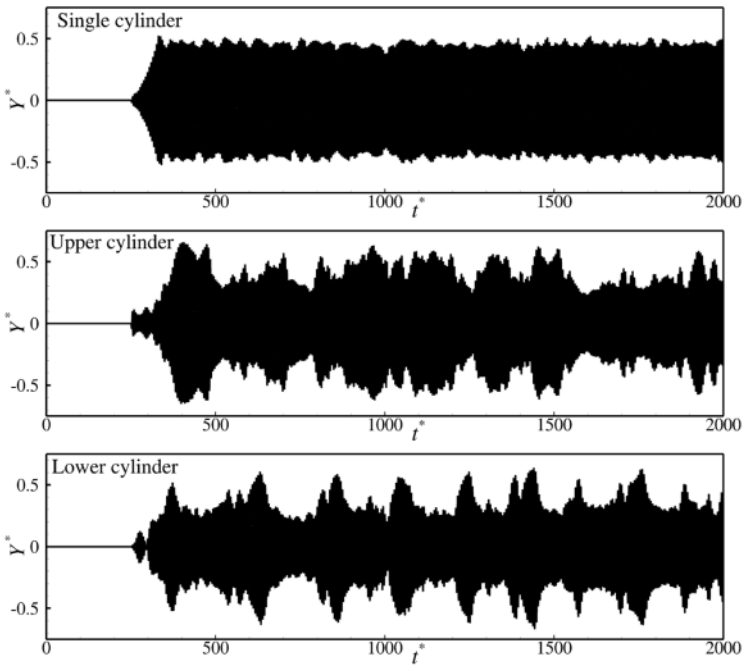

Fig. 7. Time series data of the cylinder displacement at U_R^* = 5.0 for single and SBS cylinders (g^* = 1.5) cases.

3-D DNS to study the characteristic flow past SBS cylinders at Re = 500 and the effect of cylinder length on the switching behaviour of gap flow between SBS cylinders. Flow regimes in the tested gap ratio were divided into five types: single bluff body flow, deflected flow, flip-flopping flow, hybrid flow, and anti-phase flow. The vortex shedding frequency and fluid forces varied significantly within each flow regime. Furthermore, the longer switching duration in the flip-flopping regime was caused by an increase in cylinder length. The VIV of SBS cylinders is also an interesting research topic considering the many applications of SBS configuration in the real world, such as heat exchanger pipes, underwater cables, offshore structures, and risers. Jiang et al. (2021) conducted an experimental study to investigate the effectiveness of triple-helical strakes in suppressing VIV of SBS risers. They found that the maximum suppression in cross-flow and in-line directions were 14.64% and 35.41%. Neumeister et al. (2021) performed VIV measurements for single and multiple cylinder configurations and observed the appearance of a bistable flow in the SBS configuration. In addition, the bistable flow was strongly influenced by the gap between SBS cylinders. Based on their investigation, Vedeld and Nestegård (2021) reported that the smaller gap between SBS cylinders forms a unique

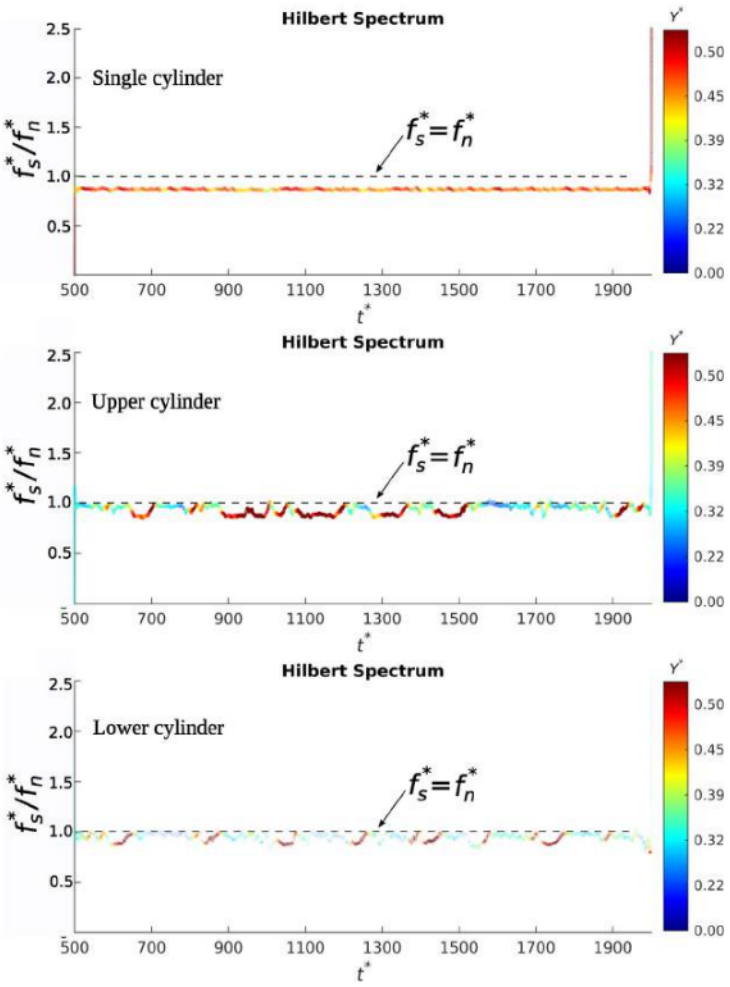

Fig. 8. HHT analysis of the time series data of cylinder displacement at $U_R^* = 5.0$ for single-cylinder and SBS cylinders ($g^* = 1.5$) cases.

Table 1
Output parameters for data analysis in a dimensionless form.

Parameter	Description
$t^* = \frac{tU_\infty}{D}$	Dimensionless time
$C_D = \frac{2F_x}{\rho U_\infty^2 DL}$	Drag coefficient
$C_L = \frac{2F_y}{\rho U_\infty^2 DL}$	Lift coefficient
$Y^* = \frac{Y}{D}$	Dimensionless transverse displacement
$A^* = \sqrt{2}Y_{\text{rms}}^*$	Dimensionless vibration amplitude
$f_v^* = \frac{f_v D}{U_\infty}$	Strouhal frequency
$f_s^* = \frac{f_s D}{U_\infty}$	Dimensionless structure frequency
$A_t(t^*)$	Autocorrelation function
η VIVACE	Efficiency of VIVACE

asymmetric wake comprised of narrow and wide wake regions near the SBS cylinders. This pattern appears before the wakes merge and create a unified wide wake in the far wake region of SBS cylinders.

Chen et al. (2020) employed 2-D numerical simulation with immersed boundary (IB) technique to investigate the VIV of a pair of cylinders in the SBS arrangement. The SBS cylinders are limited to vibrate in the cross-flow direction with the gap ratio $g^* = g/D$ in the range $1.0 \leq g^* \leq 4.0$, where g represents the gap (surface-to-surface distance) between SBS cylinders. This simulation was performed for Re = 60–200 and $U_R^* = 2.0$–10.0. This study found a significant gap ratio influence, especially for amplitude and frequency responses from SBS cylinders. Other significant discoveries for the SBS cylinders were the extended lock-in region and the formation of several harmonic frequencies. Using the same 2-D numerical simulation, Zou et al. (2021) investigated the effect of cylinder arrangement and constraint on VIV responses of two cylinders at Re = 100. The cylinder arrangements used in this study were SBS, tandem, and staggered configurations with $g^* = 1$. Moreover, the existence of cylinder constraint in this study forced two cylinders to move in the same direction. The results from all arrangements with constraint showed the significant suppression of VIV when $U_R^* < 7$. For cases with $U_R^* > 7$, the VIV response of the SBS arrangement with constraint was enhanced. Lastly, the wake pattern of the two cylinders with constraint was more stable for all cylinder arrangements. For the study with three-dimensional (3-D) numerical simulation involving the VIV phenomena in an SBS arrangement, Liu

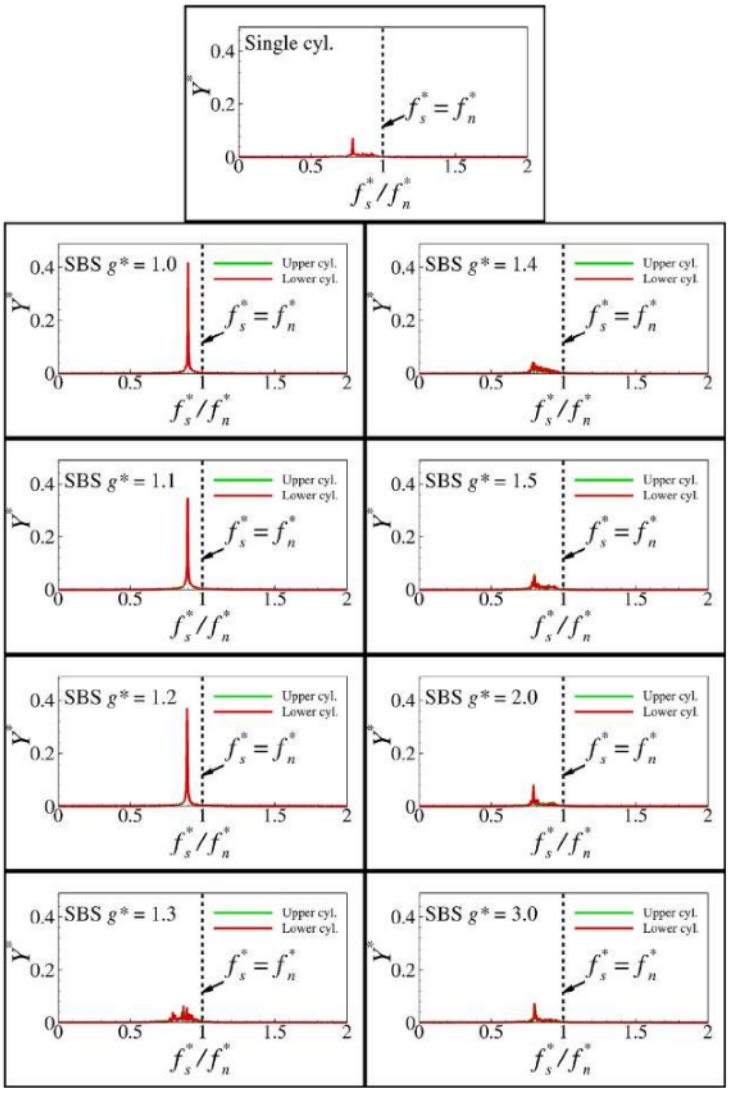

Fig. 9. Frequency response of the single-cylinder and SBS cases with different gap ratios at $U_R^* = 4.0$.

and Jaiman (2018) investigated the relation of the gap between the SBS cylinders and the VIV response at Re = 500. In this study, only the upper cylinder could oscillate in the cross-flow direction with following VIV parameters: $U_R^* = 2.0–10.0$, $m^* = 10.0$ and $\zeta = 0.01$. This investigation was performed for the range of gap ratios $0.3 < g^* < 3.0$. It was found that the upper cylinder started the lock-in earlier compared to the VIV case of a single-cylinder. Furthermore, the gap ratio between upper and lower cylinders enhanced the instability of vortex interaction. This finding is important for operations as well as design perspectives of offshore structures. Munir et al. (2019) used DNS to investigate the influence of g^* on the VIV of two rigidly constrained SBS cylinders at Re = 1,000. This study was performed for the range of reduced velocities $1 < U_R^* < 20$ with $m^* = 2.0$. and $\zeta = 0$. The VIV responses were analysed for $g^* = 0.5$ to 3.0. They found that the high vibration amplitude response spectrum is separated into two zones for small gap ratios: lock-in and sub-harmonic. The sub-harmonic area is defined as a region where the oscillation frequency is half of the lift coefficient frequency. The interaction between the cylinders was quite strong for $g^* = 0.5$, as indicated by a longer lock-in area and a greater amplitude. Furthermore, the behaviour of the two cylinders was found to be identical for $g^* = 3$.

Nowadays, not many investigations have been conducted on the VIV of two cylinders in the SBS configuration, particularly for 3-D numerical simulation with freely vibrating SBS cylinders at higher Reynolds numbers. Liu and Jaiman (2018) conducted a similar study but only focused on the VIV responses of the upper cylinder while keeping the lower cylinder as a fixed structure. Another comparable study performed by Munir et al. (2019) also did not focus on the free vibration of SBS cylinders. They gave constrained the SBS cylinders so that they always vibrated together. Recently, many researchers have investigated the VIV response of multiple cylinders for the purposes of energy harvesting systems such as VIVACE. Several experimental and numerical studies on VIVACE (Lv et al., 2021a; Ding et al., 2021; Lee et al., 2021; Yuan et al., 2021; Li et al., 2021) have investigated the performance of multiple cylinders in a tandem configuration. Nevertheless, there is an opportunity to investigate the VIV response of the SBS cylinder and

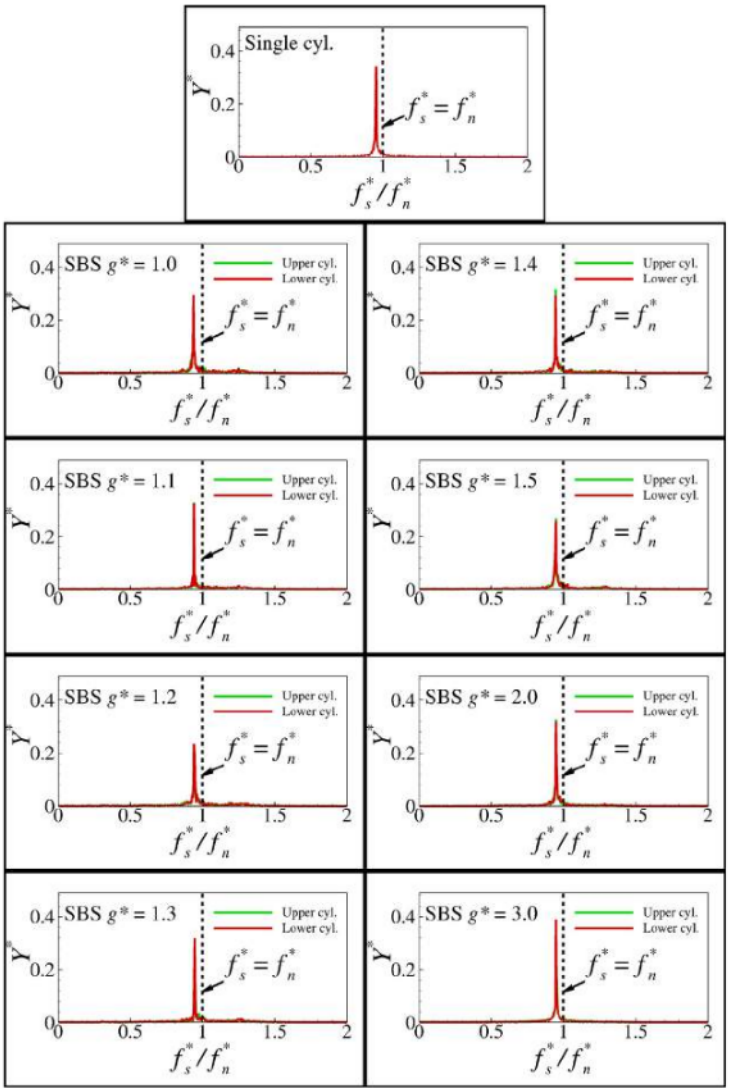

Fig. 10. Frequency response of the single-cylinder and SBS cases with different gap ratios at $U_R^* = 6.0$.

specifically to find the characteristics of the SBS configuration in a VIVACE system. The present study performs a 3-D numerical simulation of two elastically mounted circular cylinders in SBS arrangement to investigate the VIV response and VIVACE performance of this configuration. This study is performed at Re = 1,000 with the following VIV parameters: $m^* = 10.0$, $\zeta = 0.01$, $U_R^* = 2.0$ to 10.0. The VIV response of the SBS cylinders is investigated in the range of gap ratio $1.0 < g^* < 3.0$. Moreover, the response correlation and the efficiency of VIVACE from the SBS cylinders are determined to assess the potential of this configuration when applied to the VIVACE system. A constant Reynolds number is employed for this present study to minimize high computing expenses for multiple cases in 3-D simulation. In this study, 105 three-dimensional numerical simulations were carried out, including nine cases for the validation section, six cases for the grid independence test, 10 cases for VIV simulation of a single-cylinder, and 80 cases for the primary investigation of the SBS cylinders undergoing VIV.

2. Research methodology

2.1. Numerical method for incompressible fluid flow

An in-house solver based on the finite volume method, named TIGER-C, was coded in C++. A modified direct-forcing immersed boundary (DFIB) technique was used to model the solid cylinders, which was earlier used by Chern et al. (2014) in a 2-D study. Later, Raza et al. (2020) also used the same approach for 3-D investigations of VIV over spheres at Re = 300. The present investigation was performed at Re = 1,000. In this regime, the turbulent wake was observed (Zhao et al., 2014). To incorporate the presence of this turbulent wake, the incompressible filtered Navier–Stokes and continuity equations based on the Large Eddy Simulation (LES), as shown in Eqs. (1)–(2) were used as the governing equation for the incompressible fluid flow problem.

$$\frac{\partial \bar{\mathbf{u}}}{\partial t} + \nabla \cdot (\bar{\mathbf{u}}\bar{\mathbf{u}}) = -\frac{1}{\rho}\nabla p + \left(\nu + \nu_t\right)\nabla^2 \bar{\mathbf{u}} + \eta \mathbf{f} \tag{1}$$

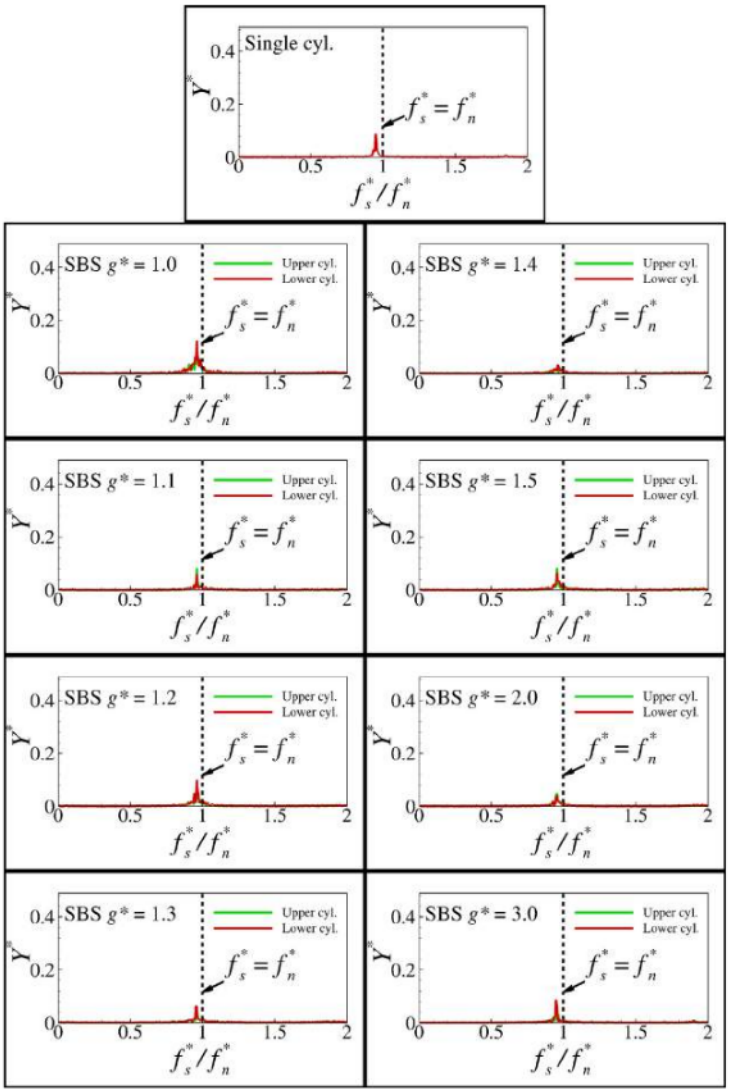

Fig. 11. Frequency response of the single-cylinder and SBS cases with different gap ratios at U_R^* = 9.0.

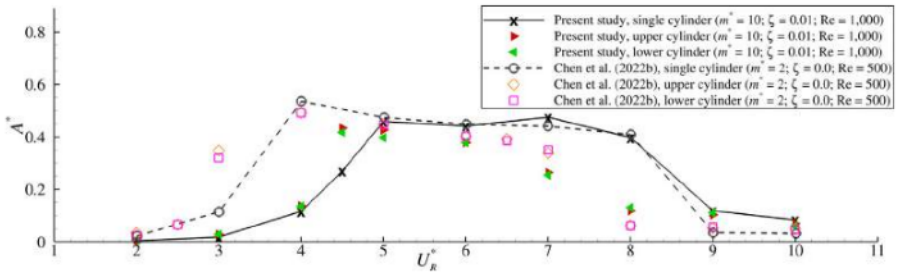

Fig. 12. Amplitude response from SBS cylinders case with g^* = 1.5 and single cylinder case in the range of U_R^*.

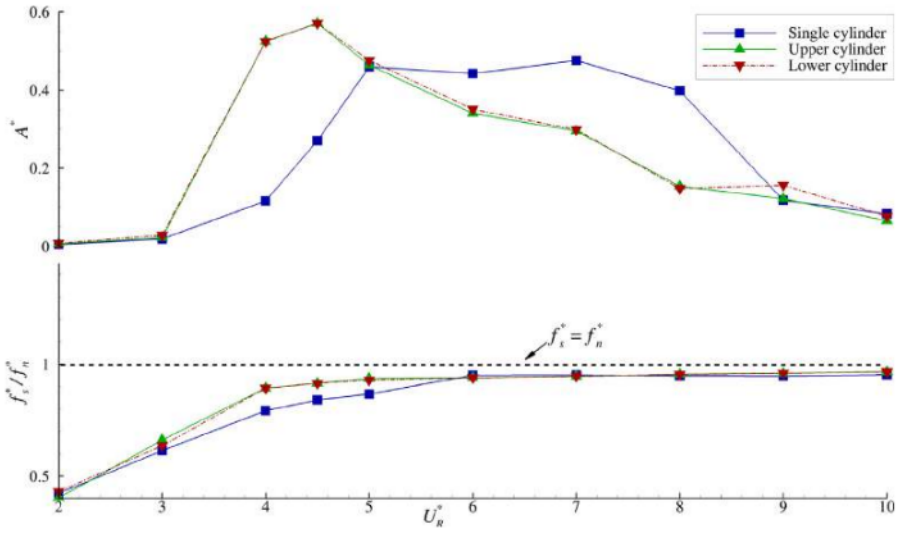

Fig. 13. Comparison of amplitude and frequency responses between SBS cylinders case with $g^* = 1.2$ and single cylinder case in the range of U_R^*.

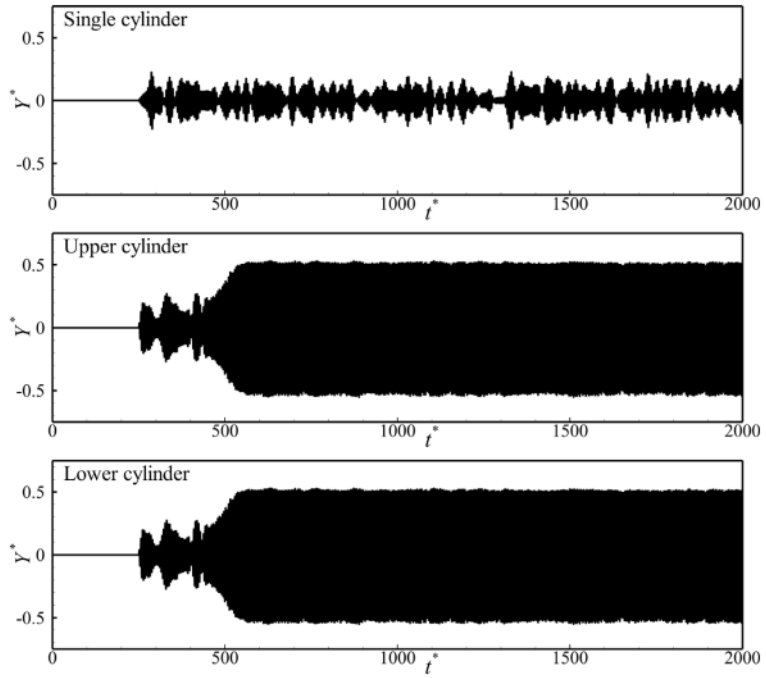

Fig. 14. Time series data of the cylinder displacement at $U_R^* = 4.0$ for single and SBS cylinders ($g^* = 1.2$) cases.

$$\nabla \cdot \bar{\mathbf{u}} = 0 \tag{2}$$

In these equations, $\bar{\mathbf{u}}$, ρ, p, and ∇ represent the filtered velocity, fluid density, pressure, and gradient operator. In the last term of Eq. (1), η represents the function of a volume of solid (VOS). This function was used to link the virtual force $\mathbf{f}$ in this DFIB technique. In this approach, $\eta = 1$ means the grid is occupied by a solid and $\eta = 0$ means the grid is filled by a fluid. In order to get the finer solid boundary, the subgrid technique was employed to calculate the η function (Raza et al., 2020, 2021). Details information about the DFIB and subgrid technique can be found in the following papers (Noor et al., 2009; Chern et al., 2014; Raza et al., 2020, 2021). In the diffusion term, ν_t represents the turbulent viscosity. In the present study, this term was determined using the Smagorinsky–Lilly model,

$$\nu_t = (C_s \Delta)^2 |\bar{S}| \tag{3}$$

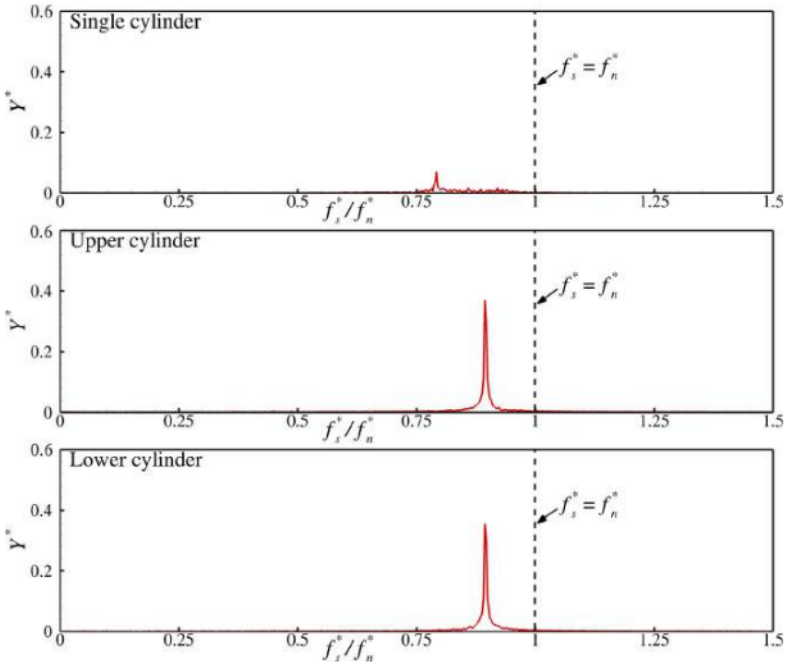

Fig. 15. FFT analysis of the time series data of cylinder displacement at $U_R^* = 4.0$ for single-cylinder and SBS cylinders ($g^* = 1.2$) cases.

$$\bar{S} = \sqrt{S_{ij} S_{ij}} \tag{4}$$

where C_s represents the Smagorinsky constant ($C_s = 0.1$), Δ is the filter width ($\Delta = (\Delta x \Delta y \Delta z)^{\frac{1}{3}}$), $\bar{S}_{ij}$ is the rate of strain of resolved velocity field. The 2nd order central difference scheme was used to calculate this resolved velocity field.

The convective term in Eq. (1) was calculated by using the quadratic upstream interpolation for convective kinematics (QUICK) scheme. The pressure term in Eq. (1) could be solved along with Eq. (2), resulting in the Pressure Poisson Equation. In this case, the Bi-Conjugate Gradient Stabilized (Bi-CGSTAB) method was selected to calculate the pressure field. The body force term in Eq. (1) is represented by virtual force from the DFIB technique, and the Simpson 1/3 rule was used to integrate the virtual force along the computational cell occupied by a solid. Eventually, the 3rd order Adam–Bashforth method was used to calculate the transient term in the governing equation. This current solver was successfully used to perform a 2-D FSI simulation for various problems in the laminar flow regime (Chern et al., 2012, 2013, 2015). Combining DFIB and LES to perform a 3-D numerical simulation of flow past a circular cylinder at Re = 3,900 has already been applied effectively (Raza et al., 2021).

2.2. Numerical method for solid motion

The solid-body motion in this present study was modelled using Eq. (5) (Zhao et al., 2014, 2017; Zou et al., 2021; Xu et al., 2022), where $\ddot{Y}^*$, $\dot{Y}^*$, and Y^* represent the non-dimensional structure's acceleration, velocity, and displacement in the cross-flow direction. On the right-hand side, C_L represents the coefficient of fluid force in the cross-flow direction. In the present investigation, the upper and lower cylinders were only enabled to move in the cross-flow direction (1-DOF motion).

$$\ddot{Y}^* + \frac{4\pi\zeta}{U_R^*}\dot{Y}^* + \left(\frac{2\pi}{U_R^*}\right)^2 Y^* = \frac{2C_L(t^*)}{\pi m^*} \tag{5}$$

For every time step, $\ddot{Y}^*$, $\dot{Y}^*$, and Y^* were solved by using the 4th order Runge–Kutta method (Chern et al., 2014; Raza et al., 2020; Zou et al., 2021). Furthermore, $\dot{Y}^*$ and Y^* were used to calculate the virtual force in the cross-flow direction and the new position of structure in the domain of computation. A previous study conducted by Chern et al. (2014) employed the same approach to investigate the VIV of a circular cylinder up to Re = 140. Further, Raza et al. (2020) used the same technique to model the VIV phenomenon of a spherical structure at Re = 300.

In order to speed up the calculation process, the OpenMP parallelization technique was used to distribute the calculation load for each processor's core. The computational environment for this present investigation consisted of several computation nodes at the National Center for High-Performance Computing (NCHC) Taiwan. Each computation node is equipped with Intel Xeon Gold 6148 2.40 GHz (40 cores processor). The computational time required for each single-cylinder case ranged from 13 to 20 h when the calculation used 20 cores of processors. For the case with SBS cylinders, the calculation used 40 cores of processors, and the computational time for each case ranged from 19 to 32 h.

2.3. Data analysis method

The turbulent wake behind the vibrating cylinders will induce some fluctuations in the VIV response. For the VIV of a circular cylinder at Re = 1,000, Zhao et al. (2014) recorded the VIV responses for 40 vibration cycles to capture the behaviour of the vibrating cylinder in response to the appearance of the turbulent wake. All calculation in this present study recorded and analysed data in the selected time window (t^* = 500–2,000), as shown in Fig. 1. The VIV responses were recorded for more than 100 vibration cycles in this selected time window. Fig. 1 represents the time-series data for VIV responses of a single-cylinder case at $U_R^* = 7.0$. In this figure, some fluctuations were observed for both displacement and lift coefficient. U_R^*-from-rest initial condition was selected to perform the VIV simulation. In this case, the flow past

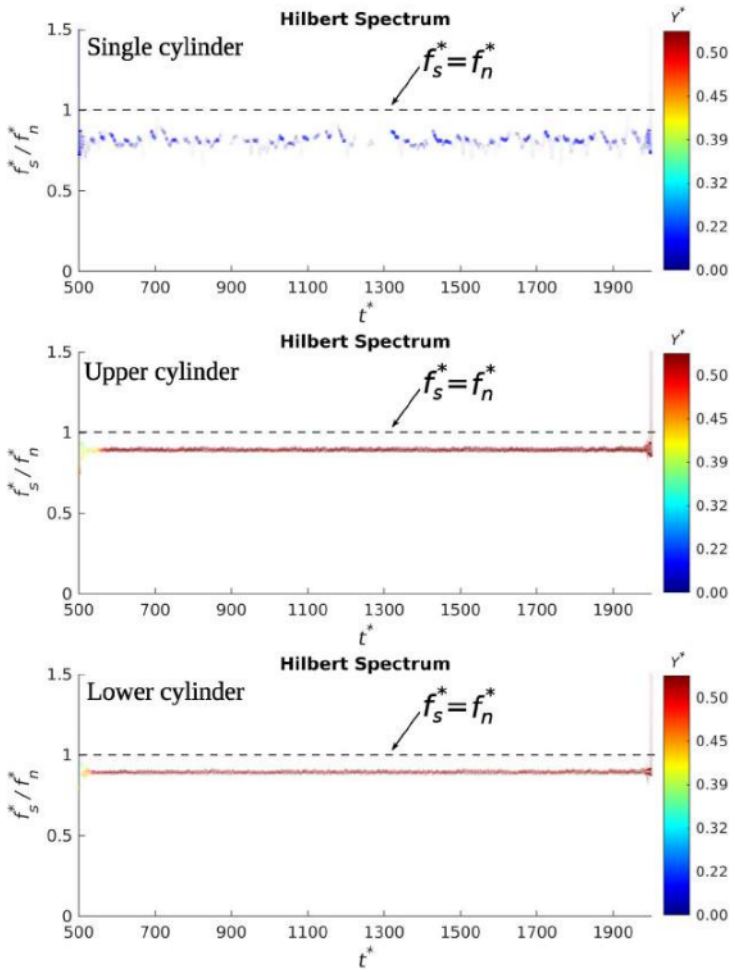

Fig. 16. HHT analysis of the time series data of cylinder displacement at $U_R^* = 4$ for single-cylinder and SBS cylinders ($g^* = 1.2$) cases.

a stationary cylinder at Re = 1,000 was performed for a time $t^* = 250$ to allow the vortex-shedding to be established (Guilmineau and Queutey, 2004). Fig. 1 also demonstrates the selected initial condition for VIV simulation, where initially the displacement was zero until $t^* = 250$. The circular cylinder was enabled to vibrate after the lift coefficient oscillated regularly.

Table 1 shows all the dimensionless parameters for data analysis in the present investigation. Herein, t and L are the simulation time and the length of a circular cylinder. The terms F_x and F_y denote the virtual force in the flow and cross-flow directions. The frequency responses f_s and f_v represent the frequency of structure vibration and vortex-shedding. The frequency responses were analysed using Fast Fourier Transform (FFT) and Hilbert–Huang Transform (HHT). Some variations in the time-series data may occasionally bring multiple harmonics due to the turbulent wake downstream of the cylinder. To overcome this problem, the dominant harmonic of the time-series signal was obtained using FFT and HHT. Hilbert Spectrum from HHT gives information about the instantaneous frequency and instantaneous amplitude (Huang and Shen, 2014). The autocorrelation function $A(t^*)$ was utilized to determine the relationship between the VIV response from lower and upper cylinders. For time-series data of lower and upper cylinders, the autocorrelation $A(t^*)$ was calculated using the following equations (Chern et al., 2010, 2015).

$$A(t^*) = \frac{\overline{Y_U^* Y_L^*}}{(Y_U^*)^2}. \tag{6}$$

$$\overline{Y_U^* Y_L^*} = \lim_{t_f^* \to \infty} \frac{1}{t_f^* - t_i^*} \int_{t_i^*}^{t_f^*} Y_U^*(t^*) Y_L^*(t^*) \mathrm{d}t^* \tag{7}$$

$$\overline{(Y_U^*)^2} = \lim_{t_f^* \to \infty} \frac{1}{t_f^* - t_i^*} \int_{t_i^*}^{t_f^*} (Y_U^*(t^*))^2 \mathrm{d}t^* \tag{8}$$

Herein, t_i^* and t_f^* indicate the initial and final time. The subscripts U and L stand for upper and lower cylinders. The result of autocorrelation functions $A(t^*)$ close to 1 represents the in-phase correlation, where two-cylinder move in the same direction. If $A(t^*)$ approaches -1, the two cylinders are in the anti-phase correlation. In this case, the two cylinders move in the opposite direction. Furthermore, if the result of $A(t^*)$ approaches zero, then the VIV response of the upper and lower cylinder are uncorrelated. The quantity of energy obtained from the available energy in the fluid flow was represented by the efficiency. The following equation evaluates the power conversion from fluid flow by the vibrating cylinder during one vibration cycle (Ding et al., 2016).

$$P_{VIVACE} = 8\pi^3 m_s \zeta f_n A^2 f_s^2 \tag{9}$$

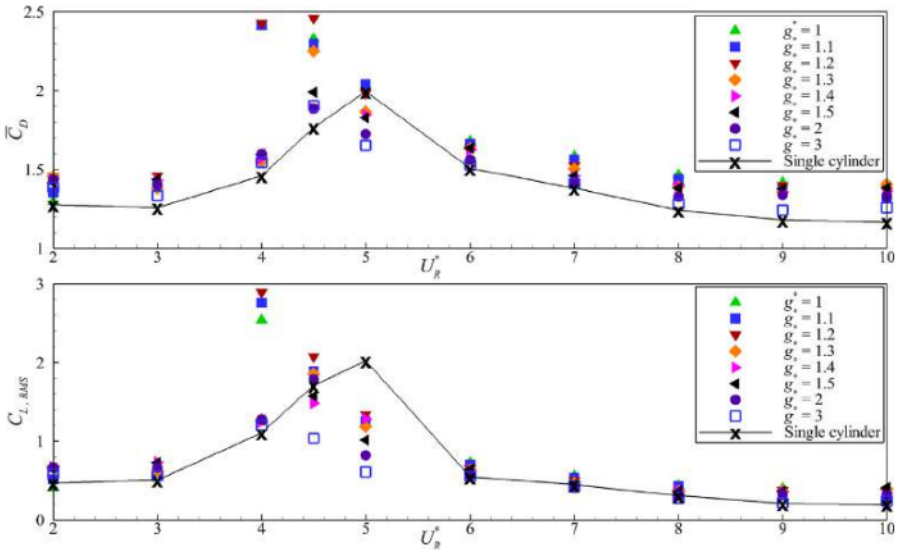

Fig. 17. Hydrodynamic force response for VIV of two cylinders in the SBS arrangement in the range of U_R^*.

The accessible power in a fluid flow can be calculated by using Eq. (10). Here, the reference power in the fluid is expressed using the total area covered by the vibrating cylinder ($[2A + D]L$) instead of a stationary cylinder (DL).

$$P_{fluid} = \frac{1}{2}\rho U_\infty^3 (2A + D)L \tag{10}$$

In the calculation of VIVACE efficiency, Kim and Bernitsas (2016) included the Betz limit (16/27), which is the theoretical maximum power that can be obtained from a fluid flow. In this study, the same calculation is used. As a result, the ratio of harnessed power to accessible fluid power is

$$\eta_{VIVACE} = \frac{P_{VIVACE}}{\text{Betz limit} \times P_{fluid}} = \frac{27\pi^3 m_s \zeta f_n A^2 f_s^2}{\rho U_\infty^3 (2A + D)L}. \tag{11}$$

Substituting dimensionless variables $U_R^* = U_\infty / f_n D$, $m^* = 4m_s/\pi\rho D^2 L$, $A^* = A/D$ and $f_s^* = f_s D/U_\infty$ obtains dimensionless equation of efficiency of the VIVACE converter.

$$\eta_{VIVACE} = \frac{27\pi^4 m^* \zeta A^{*2} f_s^{*2}}{4U_R^*(2A^* + 1)}. \tag{12}$$

3. Computational domain and boundary conditions

Fig. 2 represents the computational domain of this present study. The total dimension in the flow direction (x) was $50D$, where $20D$ and $30D$ were placed in upstream and downstream of the center of SBS cylinders. The total dimension of computational domain in the flow direction is important, especially in the VIV simulation. If the dimension is too small, then the boundary condition will affect the solution. Previous VIV simulations at Re = 1,000 also employed the same dimension ($50D$) in the flow direction (Zhao et al., 2014; Munir et al., 2019). The dimension of computational domain in the cross-flow direction (y) was $40D$ and the blockage ratio ($2D/y$) for this study became 5%. Based on the previous studies, certain essential VIV responses such as lock-in and hysteresis phenomenon were identified with 5% blockage ratio (Prasanth et al., 2006, 2011). The spanwise dimension (z) of this study was $3D$ and the periodic boundary condition was implemented on the spanwise boundaries. Zhao et al. (2014) explained that the shorter spanwise length might be used with this periodic boundary condition to reduce the computational requirement. Kondo (2014) also used the shorter spanwise length ($z = 2.5D$) and periodic boundary condition to do the 3-D VIV simulation of multiple cylinders.

The boundary conditions applied in the flow direction were uniform free-stream at the inlet location and zero-gradient at the outlet position. For the cross-flow direction, the symmetry boundary condition was selected for both sides, this assumption defines a zero value for the velocity component perpendicular to the boundary. The no-slip boundary condition was applied to the solid structure through the DFIB technique. Raza et al. (2021) used the same combination of boundary conditions to simulate flow past cylinder at Re = 3900. Liu and Jaiman (2018), Pastrana et al. (2018) and Wang et al. (2017) performed 3-D VIV simulation with the same combination of boundary conditions. Fig. 2 also shows the section of the computational grid around the SBS cylinders at x–y plane, where the grid was uniformly distributed near the two cylinders. Outside the uniform grid region, the non-uniform grid was employed to reduce the total number of grids. In the spanwise direction, the uniform grid was selected with $\Delta z = 0.2D$.

4. Grid independence study

In order to obtain grid independence result in the numerical solution, several grid configurations were selected to perform VIV simulation of SBS cylinders at Re = 1,000. Fig. 3 shows the complete layout of grid composition at the x–y plane. Far from the vibrating structures, the computational grid was constructed of coarse grid regions with a non-uniform distribution. Near the vibrating structures, the fine grid region with uniform distribution in the x and y directions was employed to capture the displacement of cylinders. Table 2 shows the selected grid configurations, where each configuration is characterized by the fine grid region near the SBS cylinders in the flow direction (Δx) and cross-flow direction (Δy). The grid independence study was performed at two reduced velocities $U_R^* = 4.0$ and $U_R^* = 5.0$ with following VIV parameters: $m^* = 10.0$, $\zeta = 0.01$ and $g^* = 1.0$. The total number of elements for grids A, B and C were 0.28 million, 1.11 million and 1.72 million, respectively. The grid independence criteria was analysed based on output simulation parameters. In this case, the amplitude and frequency responses from the lower cylinder were selected for comparison. Grids B and C provided nearly similar results, with the

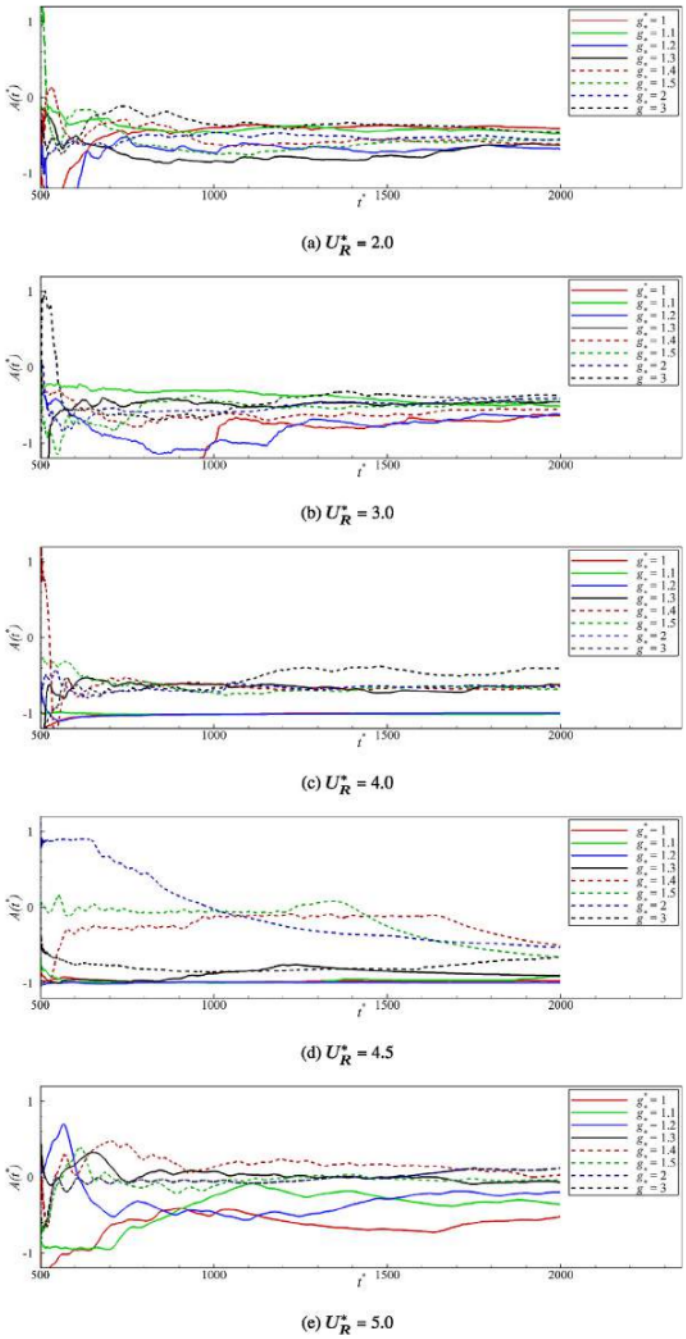

(a) $U_R^* = 2.0$

(b) $U_R^* = 3.0$

(c) $U_R^* = 4.0$

(d) $U_R^* = 4.5$

(e) $U_R^* = 5.0$

Fig. 18. Response correlation between upper and lower cylinders in the case of a SBS configuration for $U_R^* = 2.0–5.0$.

highest variation being less than 1%. As a consequence, Grid B was used in this study to achieve numerical precision while also decreasing computation costs.

5. Validation cases

The validation case of the DFIB method for 2-D VIV simulation can be found in the following papers (Chern et al., 2014, 2018). The present numerical solver has also been tested for 3-D FSI modelling in a turbulent flow as well as VIV simulation of 3-D structure (Raza et al., 2020, 2021). The VIV of an upper cylinder in SBS configuration was numerically investigated by Liu and Jaiman (2018) through 3-D numerical simulation. This problem will be used as a validation case to verify the ability of the DFIB method to simulate multiple 3-D structures undergoing VIV. The validation case was performed at Re = 500 with

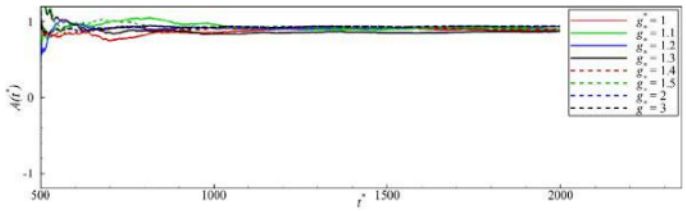

(a) $U_R^* = 6.0$

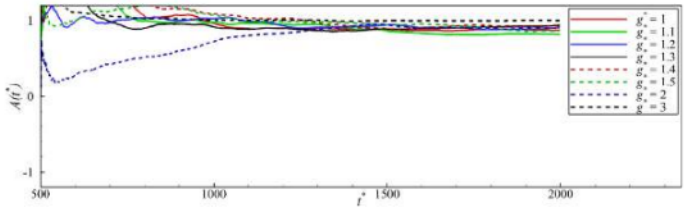

(b) $U_R^* = 7.0$

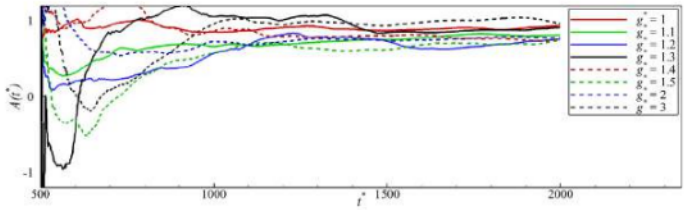

(c) $U_R^* = 8.0$

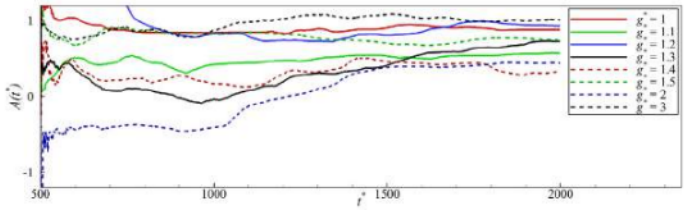

(d) $U_R^* = 9.0$

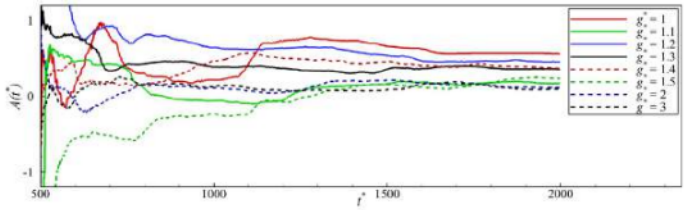

(e) $U_R^* = 10.0$

Fig. 19. Response correlation between upper and lower cylinders in the case of an SBS configuration for $U_R^* = 6.0–10.0$.

Table 2
Grid independence study (percentage error inside a bracket is calculated based on grid C).

Grid	$\Delta x \& \Delta y$	A^* at $U_R^* = 4.0$	f^* at $U_R^* = 4.0$	A^* at $U_R^* = 5.0$	f^* at $U_R^* = 5.0$
A	$0.050D$	0.3498 (27.98%)	0.8880 (1.81%)	0.4593 (2.25%)	0.9130 (1.88%)
B	$0.025D$	0.4832 (0.51%)	0.9012 (0.35%)	0.4658 (0.87%)	0.9300 (0.05%)
C	$0.020D$	0.4857	0.9044	0.4699	0.9305

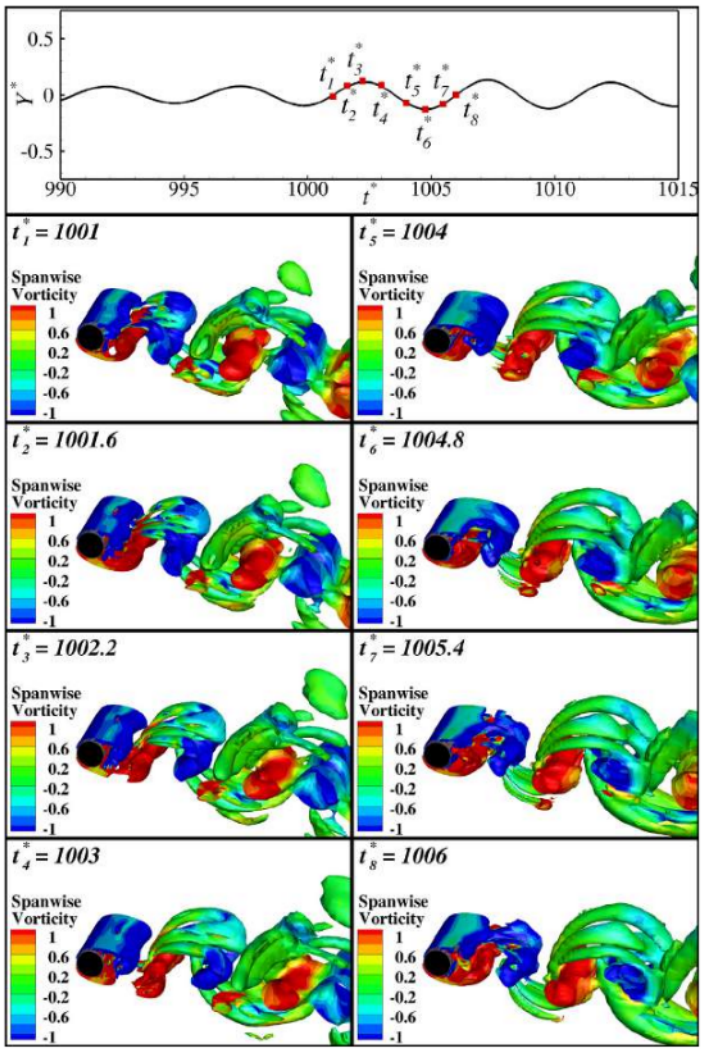

Fig. 20. Instantaneous flow field rendered and coloured by Q-criterion and spanwise vorticity for the single cylinder case at $U_R^* = 4.0$.

following simulation parameters: $U_R^* = 3.0–9.0$, $m^* = 10.0$, $\zeta = 0.01$ and $g^* = 0.8$. Liu and Jaiman (2018) solved this particular issue till $t^* = 350$ and calculated vibration responses using the time range $t^* = 250–350$ (20 vortex-shedding cycles). The vibration responses in our current investigation were calculated using the same 20 vortex-shedding cycles as in the previous investigation. This study gathered data till $t^* = 2{,}000$ (more than 200 vortex-shedding cycles) and picked 20 vortex-shedding cycles from the time-series data as the validation case. Fig. 4 shows the response comparison of present and published results. The amplitude and frequency responses of the vibrating cylinder were selected for data comparison in the validation case. The current results were in agreement with previously published results, in terms of individual value as well as response pattern in the range of reduced velocity. The verification results demonstrate that the present DFIB technique is proper and accurate in predicting the VIV phenomena with multiple structures in the SBS configuration.

The TIGER-C solver has been tested to simulate the VIV of a single cylinder in the range of $900 \leq Re \leq 15{,}000$. The same VIV parameters as the published results were used in this test case ($m^* = 2.4$, $\zeta = 0.0054$, and $U_R^* = 1.0–17.0$). In order to match the data collection method from published results, an increasing-U_R^* initial condition was employed to perform this VIV modelling. Fig. 5 shows the vibration response of a single cylinder in the range of Reynolds number. Similar to published results, the normalized maximum amplitude was used to characterize the VIV response. In this validation section, the corresponding amplitude branches (initial, upper, and lower) from Khalak and Williamson (1996) were employed. Compared with the published experimental result from Khalak and Williamson (1996), the present study showed slightly over-predict results, except for the beginning of upper and lower branches, where the present result was in good agreement. In comparison with the published numerical result from Guilmineau and Queutey (2004), the present study was in good agreement in the initial branch as well as the beginning of the lower branch. Fig. 5 shows that no numerical result accurately predicted the upper branch of the experimental results. The finite cylinder in the VIV experiment, which caused fluid flow between the cylinder tip and the channel wall, was one of the possible factors of this issue. Due to the complete elimination of the cylinder length effect, the 2D RANS simulation displayed a very different pattern on the upper branch. The 3D numerical modelling should generally produce a more accurate result, particularly in the

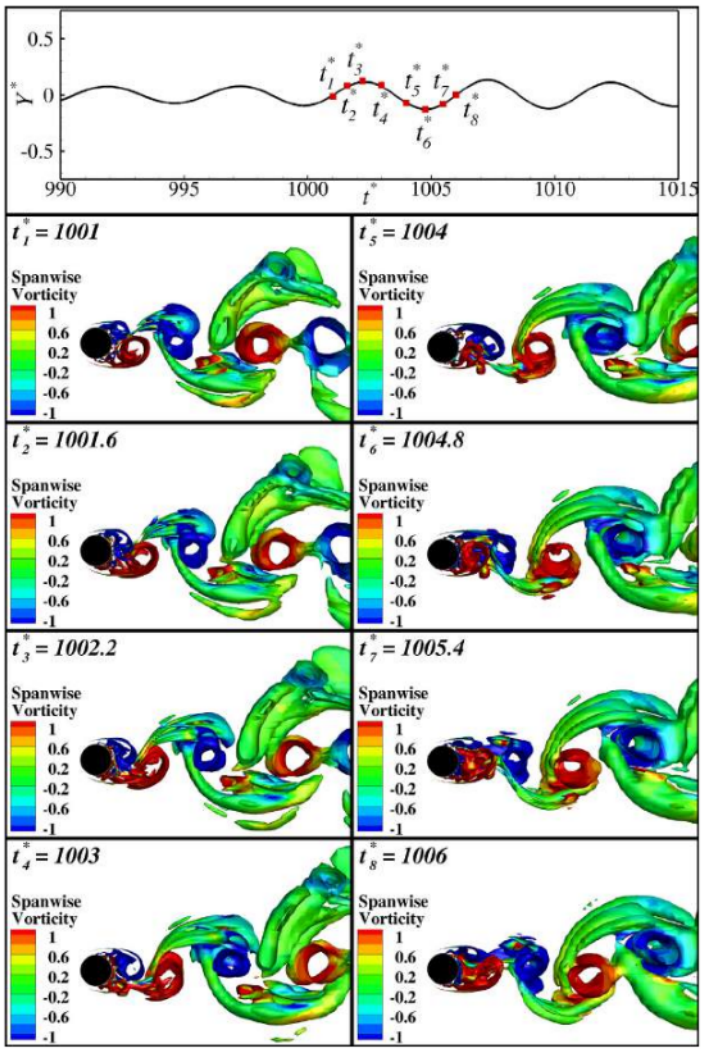

Fig. 21. Instantaneous flow field rendered and coloured by Q-criterion and spanwise vorticity for the single cylinder case at $U_R^* = 4.0$ (side view).

case of turbulent flow. At the beginning of the upper branch, this current 3D result and those from Matin Nikoo et al. (2019) both provided reliable results. Then, both results were under-predicted until the end of the upper branch. Perhaps this discrepancy is caused by the spanwise boundary condition. Symmetry conditions were chosen for the spanwise boundary of 3D RANS, while 3D LES used periodic conditions. The physical conditions in the VIV experiment were not the same for the two boundary conditions. Overall, the present numerical solver was able to capture all three branches in the VIV response, whereas the previous 2D numerical study had difficulty capturing it, especially in the upper branch.

6. Results and discussions

6.1. Vibration responses

In order to investigate the effect of the gap ratio on the vibration responses of SBS cylinders, information on all responses in the range of U_R^* is required. Fig. 6 shows variations of the amplitude and frequency response for VIV of two cylinders in a SBS arrangement with respect to U_R^*. Because the VIV responses of SBS cylinders are equal in most of the ranges of U_R^*, only the responses of a lower cylinder are shown here (Chen et al., 2020). The VIV responses of a single cylinder in Fig. 6 reveal the regime of $U_R^* < 5.0$, where the amplitude and frequency ratio increase as the reduced velocity increase, as the initial branch region; the regime of $5.0 \leq U_R^* \leq 8.0$, where the amplitude and frequency ratio almost stays in the constant value, as the upper branch region; the regime of $U_R^* > 8.0$, where the amplitude sharply decrease, and frequency ratio almost stays in the constant value, as the lower branch region. These VIV branches are used to characterize the VIV responses for this investigation. Two vibrating cylinders placed in the SBS position allow a collision if the vibration amplitude is greater than half the gap ratio. In this study, the highest vibration amplitude is $A^* = 0.57$, produced by the SBS case with $g^* = 1.2$ at $U_R^* = 4.5$. Since $A^* < 0.5g^*$, it can be ensured that no collision occurs between the vibrating cylinders. The SBS cylinders with $g^* = 1.0$–3.0 produce almost similar amplitude responses with the case of a single cylinder in the lower branch region. The effect of the gap ratio at $U_R^* = 2.0$–3.0 is not apparent, where the amplitude and frequency responses from

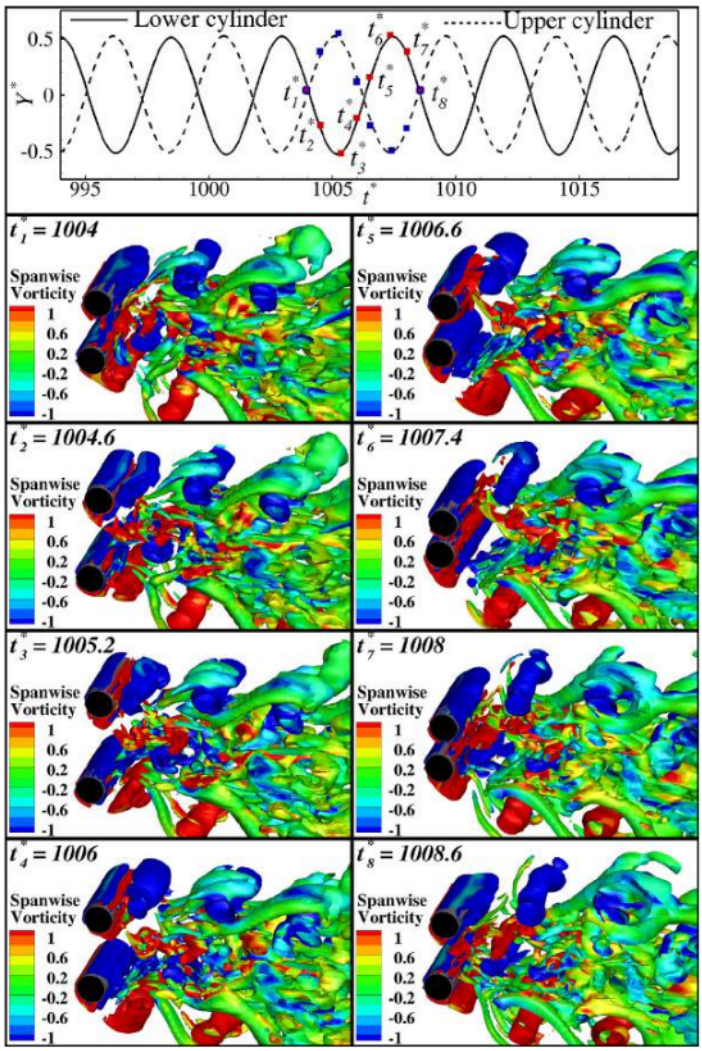

Fig. 22. Instantaneous flow field rendered and coloured by Q-criterion and spanwise vorticity for the SBS cylinders case (g^* = 1.2) at U_R^* = 4.0.

SBS cylinders and the single cylinder are almost the same. There are significant differences in amplitude response in the initial and upper branch regions. The SBS cylinders with certain gap ratios produce higher amplitude in the initial branch region. All SBS cylinder cases at U_R^* = 4.5 produce higher amplitudes, and cases with g^* = 1.0–1.3 produce much higher amplitude in this region. In the upper branch region, almost all SBS cylinder cases produce smaller amplitudes than the single cylinder response. It means the SBS arrangement reduces the flow energy conversion in this region. The amplitude response from the SBS cylinders is almost similar to the single-cylinder response at the transition point between the initial and upper branches (U_R^* = 5.0). After that, the amplitude response from the SBS cylinders is almost less than the response from the single-cylinder case. The SBS cylinders cases with g^* = 1.0–1.2 produce a slightly higher amplitude at U_R^* = 5.0 in comparison with the single cylinder amplitude. In addition, the SBS cylinders case with g^* = 3.0 produces almost the same amplitude as the single cylinder response at U_R^* = 5.0–7.0. The significant increase in the amplitude response only occurs in the initial branch region. The results from Chen et al. (2015) and Chen et al. (2020) also showed the same pattern for the VIV case of SBS cylinders at low Reynolds number (Re = 100–200). Moreover, the 3-D DNS study of vibrating SBS cylinders at Re = 500 also showed the same higher amplitude in the initial branch region (Chen et al., 2022b). In the case of a single cylinder, the VIV excitation is vortex-shedding only. But in the case of SBS cylinders, the VIV excitation also comes from the gap flow between vibrating SBS cylinders. A small gap ratio will increases fluid flow between SBS cylinders as well as the vortex-shedding frequency (Chen et al., 2022b). As shown in Fig. 6, the SBS cases show a higher frequency ratio than the single-cylinder case in the initial excitation region. A larger gap ratio reduces the effect of gap flow on VIV excitation so that the VIV response of SBS cylinders with a larger gap tends to be similar to the case of a single cylinder.

The frequency ratio of the SBS cylinders is slightly larger than that of the single cylinder in the initial branch region. This condition drives the SBS cylinders to experience an earlier onset of lock-in or synchronization phenomenon. The earlier onset of lock-in is also accompanied by the presence of the high amplitude response, where one of the characteristics of the lock-in region is the appearance of high amplitude. Liu and Jaiman (2018) also observed the same early onset of the lock-in region for VIV simulation of an upper cylinder in

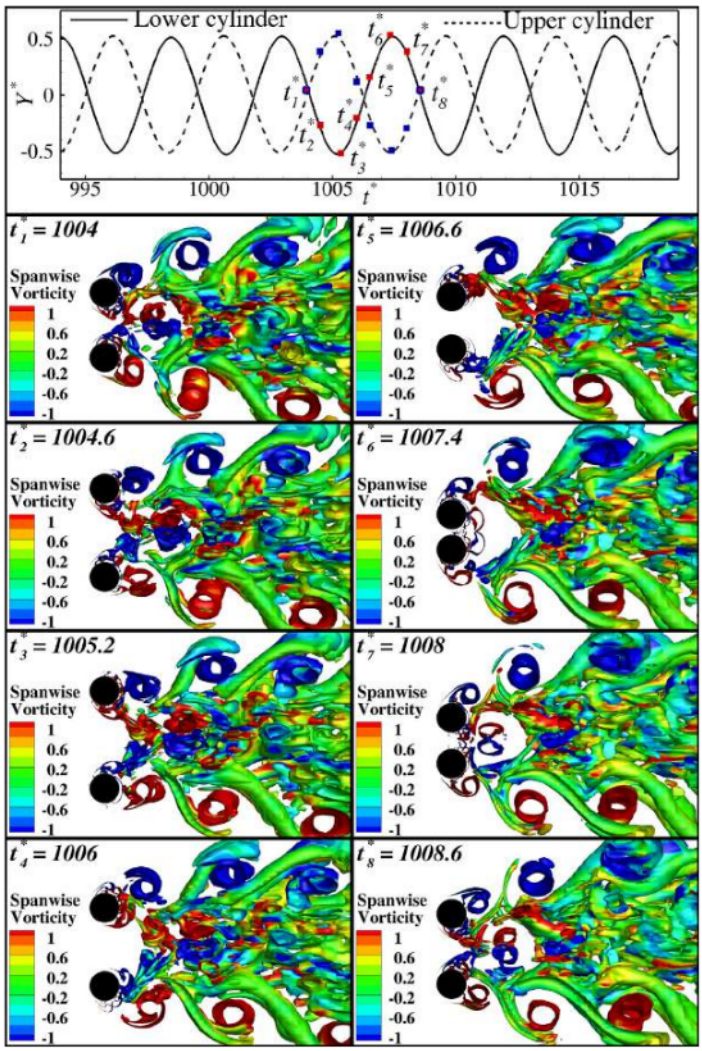

Fig. 23. Instantaneous flow field rendered and coloured by Q-criterion and spanwise vorticity for the SBS cylinders case (g^* = 1.2) at U_R^* = 4.0 (side view).

the SBS arrangement. The frequency ratio of SBS cylinders is larger than the frequency ratio from a single cylinder for all gap ratios at U_R^* = 5.0. This result contrasts with the amplitude response, where almost all gap ratios produce less amplitude. The vibration response in the time and frequency domains at U_R^* = 5.0 is presented to observe this phenomenon. Figs. 7 and 8 show the time series data and HHT analysis of the cylinder displacement at U_R^* = 5.0 for single and SBS cylinders (g^* = 1.5). Significant fluctuations arise for both time-series data from upper and lower cylinders with irregular time intervals. This phenomenon is caused by the gap between cylinders creating the disturbance or gap flow interference. This disturbance induces multiple frequencies and reduces the amplitude, as shown in Fig. 8.

Figs. 9, 10, and 11 show the frequency response of the single-cylinder and SBS cases with different gap ratios at U_R^* = 4.0, U_R^* = 6.0, and U_R^* = 9.0. Each of the presented reduced velocities is located on the initial, upper, and lower branches. For the case of SBS cylinders, the frequency response of the upper and lower cylinders shows almost identical results for all presented reduced velocities. The harmonic frequencies from the upper and lower cylinders overlap, as shown in Figs. 9, 10, and 11. At U_R^* = 9.0, the frequency responses from the single cylinder and SBS cylinders do not show a significant difference, where the harmonic frequencies are almost the same, as shown in Figs. 6 and 11. At U_R^* = 6.0, the frequency responses from the single cylinder and SBS cylinders also show identical results, where the harmonic frequencies of all cases are similar, as shown in Fig. 10. A significant difference in frequency response is observed at U_R^* = 4.0 (Fig. 9), where only the SBS cases with $g^* \geq 1.3$ show similar harmonic frequency compared to the single cylinder case. For the SBS cases with g^* = 1.0–1.2, the resulting harmonic frequency is higher than that of a single-cylinder case. As previously mentioned, the smaller g^* increases the fluid flow in the gap between the SBS cylinders as well as the frequency of vortex-shedding. The increase in vortex-shedding frequency leads the SBS cylinders to vibrate with a higher frequency. This condition drives the SBS cylinders to vibrate close to the natural frequency so that a high amplitude vibration response is observed in the case of SBS with g^* = 1.0–1.2. Chen et al. (2022b) also observed a similar increase in frequency for the VIV modelling of the SBS cylinders at Re = 500. The effect of gap flow is not significant at U_R^* = 6.0 and U_R^* = 9.0 because both reduced velocities are located in the lock-in region, so the VIV response is fully affected by vortex-shedding. The effect of

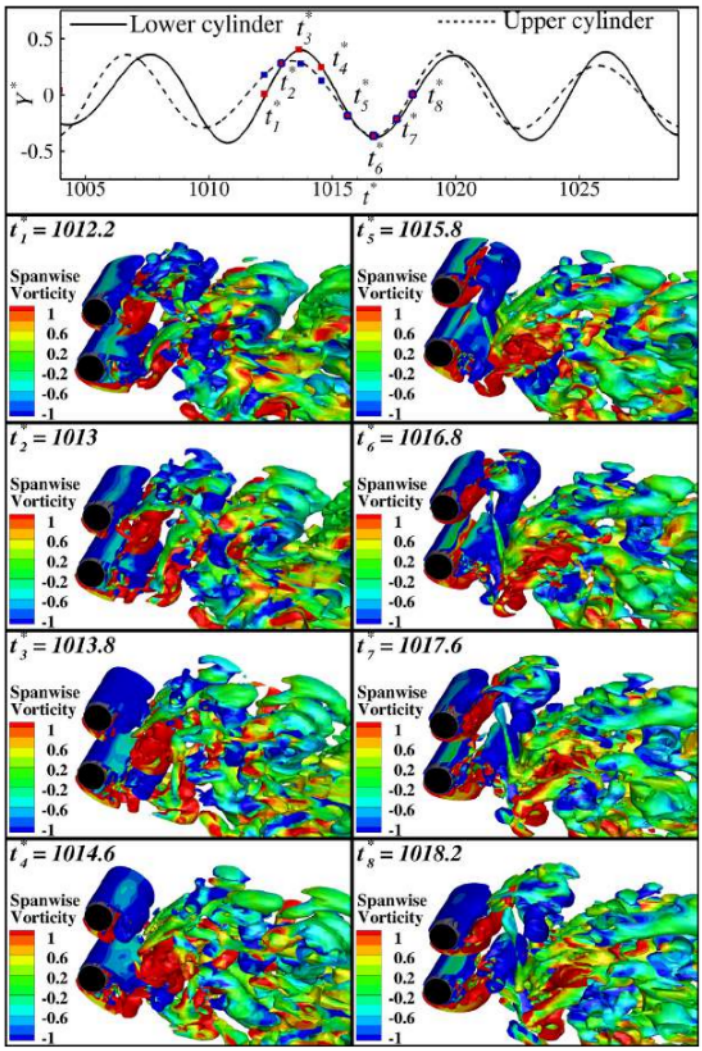

Fig. 24. Instantaneous flow field rendered and coloured by Q-criterion and spanwise vorticity for the SBS cylinders case ($g^* = 1.2$) at $U_R^* = 6.0$.

gap flow is very significant at $U_R^* = 4.0$ due to the initial excitation of VIV. In this condition, a slight disturbance in the fluid flow around the vibrating cylinders will affect the VIV response of the SBS cylinders. In this case, the disturbance comes from the gap flow between the SBS cylinders.

Chen et al. (2022b) performed 3-D DNS to study the characteristic of vibrating SBS cylinders at Re = 500 with the following VIV parameters: $m^* = 2.0$, $\zeta = 0.0$, and $U_R^* = 2.0$–10.0. Fig. 12 shows the amplitude response from SBS cylinders case with $g^* = 1.5$ and single cylinder case in the range of U_R^*. The related results from Chen et al. (2022b) with the same gap ratio $g^* = 1.5$ are presented for detailed comparison. In general, the results of the present study and Chen et al. (2022b) are different due to differences in VIV parameters and also flow conditions. Based on Fig. 12, there are similar patterns that can be observed. The SBS cylinders only showed a larger amplitude in the initial excitation region, specifically at $U_R^* = 3.0$ for the results from Chen et al. (2022b) and at $U_R^* = 4.5$ for the results from this present study. Chen et al. (2022b) concluded that the gap flow interference results in an acceleration of fluid flow between the vibrating SBS cylinders so that a significant increase in amplitude occurs at the smaller reduced velocity. This conclusion is also valid for cases with different VIV parameters and flow conditions, such as investigations that use different mass ratios, damping ratios, and Reynolds numbers. A dampening effect of SBS cylinders observed by Chen et al. (2022b) at $U_R^* = 6.0$–8.0 also can be seen clearly in the present study, as shown in Fig. 12. Overall, the influence of gap flow between vibrating SBS cylinders can be said to be similar, although the VIV parameters and flow conditions used are different.

Based on the previous investigation and our purpose in the flow energy conversion, the gap ratio $g^* = 1.2$ is observed as the optimum gap for VIV on the two cylinders in an SBS arrangement. Fig. 13 shows the comparison of vibration responses from the SBS cylinders case with $g^* = 1.2$ and single cylinder case, so that we can identify the effect of $g^* = 1.2$ on the range of U_R^*. The gap ratio $g^* = 1.2$ enhances the amplitude responses for the initial branch region ($U_R^* = 4.0$–5.0). The same gap ratio decreases the vibration response for different reduced velocities, especially in the upper branch region. The lower cylinder from the SBS cylinders at $U_R^* = 9.0$ produces a slightly higher amplitude response. The energy harvesting devices such as VIVACE require high vibration amplitude to convert flow energy into mechanical energy.

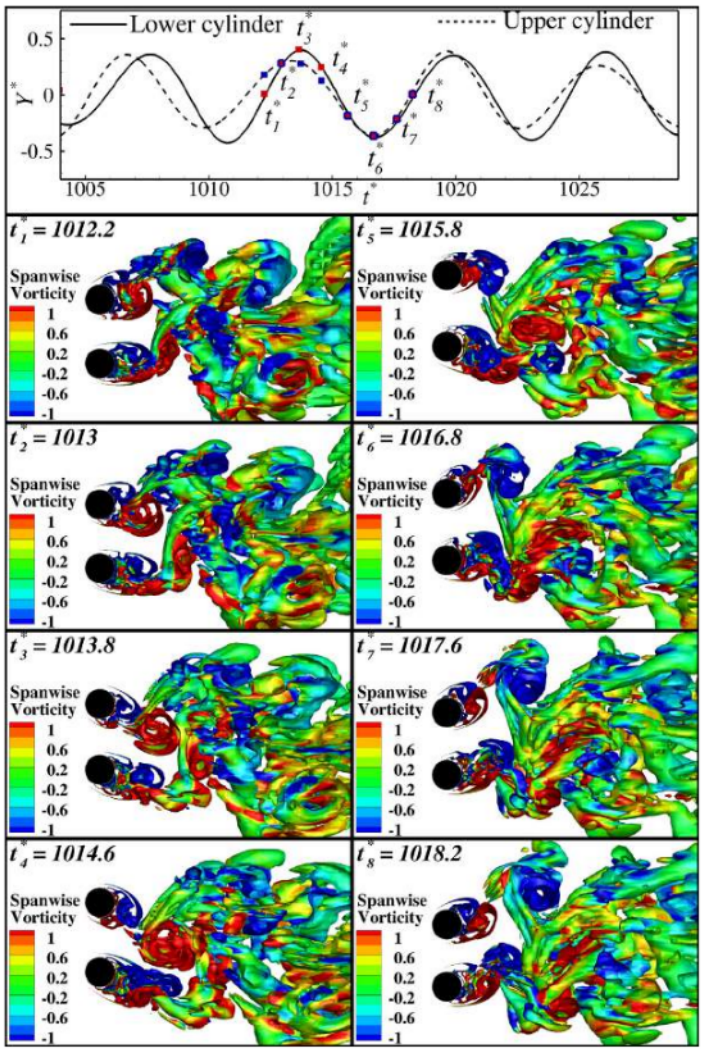

Fig. 25. Instantaneous flow field rendered and coloured by Q-criterion and spanwise vorticity for the SBS cylinders case ($g^* = 1.2$) at $U_R^* = 6.0$ (side view).

In this situation, the SBS cylinders would give better performance for VIVACE in the range of reduced velocity $U_R^* = 4.0$–5.0. More details about VIVACE efficiency analysis will be discussed in the following next section.

The early onset of lock-in phenomenon for SBS cylinders case with $g^* = 1.2$ is clearly observed in Fig. 13. The SBS cylinders with $g^* = 1.2$ start lock-in at $U_R^* = 4.0$. This lock-in region occurs earlier compared with the case of the single cylinder, which starts lock-in at $U_R^* = 5.0$. The observation of the time series data and its harmonic shows how the gap flow interference between SBS cylinders shifts the lock-in region. The time-series data of the cylinder displacement from single and SBS cylinders ($g^* = 1.2$) cases are compared to identify the effect of gap flow between cylinders. In addition, the comparison of frequency analysis from FFT and HHT for both cases is presented to see the harmonic frequency for each case.

Fig. 14 shows the time series data of the cylinder displacement at $U_R^* = 4.0$ for both single and SBS cylinders with $g^* = 1.2$ cases. A significant difference appears in the time series data of cylinder displacement. The case of a single cylinder shows fluctuating time-series data of cylinder displacement with lower amplitude. In the SBS cylinders case, the fluctuation only occurs for a moment after the rest initial condition. After that, the cylinder displacement jumps to a higher amplitude with an almost uniform peak. The time-series data from cylinder displacement show the behaviour of the vibrating cylinder in response to the flow condition near the cylinder. In order to identify the frequency response of the vibrating cylinder, the harmonic frequency from each time series data is analysed together with the natural frequency from the vibrating cylinder.

Figs. 15 and 16 represent FFT and HHT analyses of the time series data of cylinder displacement at $U_R^* = 4.0$ for single cylinder and SBS cylinders ($g^* = 1.2$) cases. The dashed line on FFT and HHT analyses represents the synchronization phenomenon, where the vibration frequency matches the natural frequency of the vibrating cylinder in the related reduced velocity. In Fig. 15, the harmonic frequency and its amplitude from the single cylinder case are less than the SBS cylinders. In HHT analysis (Fig. 16), the significant fluctuation of instantaneous frequency from the single-cylinder case is observed, whereas the instantaneous frequency from the SBS cylinders is almost in the constant value. The harmonic frequency from single-cylinder case is $f_s^* = 0.198$

and the harmonic frequencies from both upper and lower cylinders in a SBS arrangement are $f_s^* = 0.2233$. The frequency ratio (f_s^*/f_n^*) for single and SBS cylinders are 0.7930 and 0.8932, where the frequency ratio equal to one means the vibrating structure enters into the synchronization with fluid flow. This investigation shows the ability of the SBS arrangement to start the lock-in earlier compared with a single-cylinder case. In this case, the SBS cylinders experience soft lock-in, where the frequency ratio is slightly smaller than one (Navrose and Mittal, 2013). Some researchers in the field of VIV also observed the frequency ratio in the lock-in region is slightly larger than one (Khalak and Williamson, 1997; Pastrana et al., 2018).

The information on hydrodynamic force response due to altering reduced velocity is required to investigate the effect of gap ratio in the hydrodynamic force response of SBS cylinders. Fig. 17 presents the average value of lift and drag coefficients for VIV of two cylinders in an SBS arrangement. The time average and root mean square average is used for drag and lift coefficients in the selected time window. Almost all gap ratios produce higher lift and drag coefficients, except for the cases at $U_R^* = 4.5$ and 5.0, where some gap ratios have smaller force coefficients. The significant increase in drag coefficient occurs at $U_R^* = 4.0$ and 4.5. In the lift coefficient result, the significant increase is observed only at $U_R^* = 4.0$ with a small gap ratio. The substantial difference in hydrodynamic force responses is observed only in the range of $4.0 \leq U_R^* \leq 5.0$ (initial branch region). At $U_R^* = 4.0$, the hydrodynamic force responses from SBS cylinder cases become similar to the responses from the single cylinder after $g^* = 1.3$. It turns out that only SBS cases with $g^* = 1.0$–1.2 significantly enhance the hydrodynamic force responses. The higher vibration amplitude from the SBS cylinders comes from a higher lift coefficient at the initial branch region. At the upper branch region, the lower lift coefficient can have a higher vibration amplitude because of the synchronization between vortex-shedding and natural frequencies of the vibrating cylinder. Because the vibrating cylinder stores energy, even a small lift coefficient can induce significant vibration amplitude in the upper branch region. Based on these results, it is observed that the peak values of drag and lift coefficients are shifted for the SBS cylinders compared with the case of a single cylinder. This phenomenon is similar to the early onset of the lock-in region in the displacement and frequency responses.

6.2. Response correlation between two SBS cylinders

Figs. 18 and 19 show the autocorrelation function for upper and lower cylinders in a SBS arrangement in the different U_R^* as well as g^*. The autocorrelation analysis is performed in the displacement response for upper and lower cylinders for the selected time window. The response correlation for $U_R^* = 2.0$ and 3.0 (see Figs. 18(a) and 18(b)) show the anti-phase correlation for all gap ratios. These results indicate no significant effect of changing g^* in the SBS cases with $U_R^* = 2.0$ and 3.0. This result is also in accordance with the results in Fig. 6 where the amplitude and frequency responses of SBS cylinders at $U_R^* = 2.0$ and 3.0 are not changed with respect to g^*.

Figs. 18(c) and 18(d) show the response correlation of SBS cylinders at $U_R^* = 4.0$ and 4.5. In this situation, SBS cylinders with $g* = 1.0$–1.2 exhibit perfect anti-phase. The perfect anti-phase correlation is defined by the value $A(t*) = 1$, and the straight line appears along the simulation time. As illustrated in Fig. 6, this perfect anti-phase correlation significantly increases the amplitude response of SBS cylinders at $U_R^* = 4.0$ and 4.5. In Fig. 18(e), the autocorrelation result of SBS cylinders for all gap ratios at $U_R^* = 5.0$ are close to zero, which means the vibration responses are almost uncorrelated. In Fig. 6, the transition point between initial and upper branch regions occur at $U_R^* = 5.0$. Similar behaviour is also observed in the response correlation analysis, where the transition from anti-phase to in-phase correlations occurs at $U_R^* = 5.0$. In the upper branch region ($U_R^* = 6.0$ and 7.0), the autocorrelation functions from SBS cylinders are close to one or in the in-phase correlation, all gap ratios exhibit almost identical response correlations. We can find that the gap ratio has no substantial influence on the response correlation of SBS cylinders, particularly in the upper branch region. As presented in Fig. 6, the in-phase correlation produces a smaller amplitude response. In the lower branch region, the autocorrelation functions show the uncorrelated response where the autocorrelation function moves close to zero for the higher reduced velocity. Based on this result, the vibration response of two cylinders in an SBS arrangement shows the anti-phase correlation at the lower U_R^*, and then the response becomes in-phase as U_R^* increases until it achieves the lock-in region. After that, the vibration response becomes uncorrelated for the higher U_R^*. The vibration amplitude is significantly increased due to the anti-phase correlation. In contrast, especially in the lock-in region, the in-phase correlation does not increase or even decrease the amplitude response.

Figs. 20 and 21 show the Instantaneous flow field rendered and coloured by Q-criterion and spanwise vorticity for the single-cylinder case at $U_R^* = 4.0$ in the 3-D isometric and side views. Within a single vibration cycle, eight instantaneous flow fields are chosen to observe the wake pattern as well as the vortex-shedding modes. The iso-surface of the Q-criterion with three particular values: 0.001, 0.01, and 0.05 are used to generate the instantaneous flow field. The vortex structure is then coloured with spanwise vorticity using a specific range (−1.0 to 1.0) to distinguish positive and negative vorticities. A red square symbol denotes the specific time of the specified instantaneous flow field in the time series data. In this case, the VIV response of a single-cylinder at $U_R^* = 4.0$ is in the initial excitation branch. This flow field clearly shows the turbulent wake structure behind the cylinder, which is similar to the results provided by Zhao et al. (2014). The 2-S (2-Single) vortex-shedding mode is observed in this particular case, where the negative and positive vortices are shed from the vibrating cylinder for one vibration cycle. Previous numerical studies for VIV of a single-cylinder at Re = 1,000 also found the same vortex-shedding mode for cases in the initial excitation branch (Navrose and Mittal, 2013; Zhao et al., 2014).

Figs. 22–25 show the instantaneous flow field rendered and coloured by Q-criterion and spanwise vorticity for the SBS cylinders case ($g^* = 1.2$) at $U_R^* = 4.0$ and $U_R^* = 6.0$ in the 3-D isometric and side views. The same values of Q-criterion, spanwise vorticity, and the number of instantaneous flow fields are selected according to the previous flow field from a single-cylinder case. The only difference is the time range of selected flow fields from time-series data due to the different vibration frequencies in each case. In Figs. The location of the instantaneous flow field of the lower and upper cylinders is shown by square symbols in red and blue. The vortex-shedding mode for the case of SBS cylinders is hard to define because the vortex structures from two SBS cylinders are immediately merged after shedding. The vortex-shedding pattern from the case of SBS cylinders is consistent with the correlation response from upper and lower cylinders. In Figs. 22 and 23, the anti-phase vortex-shedding pattern is observed, where the vortices from upper and lower cylinders are shed in the opposite direction. The same pattern is observed for the response correlation of SBS cylinders ($g^* = 1.2$) at $U_R^* = 4.0$, as shown in Fig. 18(c). In this condition, the gap between vibrating SBS cylinders will become smaller when the upper cylinder moves down and the lower cylinder moves up, so the fluid flow in the gap will increase, and the pressure will decrease. This pressure drop in the gap will significantly increase the lift force of the vibrating SBS cylinder, as shown in Fig. 17, where $C_{L.RMS}$ value for the SBS case with $g^* = 1.2$ reaches the highest value at $U_R^* = 4.0$. Furthermore, for the anti-phase pattern, the upper and lower cylinders have the possibility to collide if the gap ratio is too small, as shown in Figs. 22 and 23 for $t_6^* = 1{,}007.4$. The in-phase vortex-shedding pattern where the vortices from upper and lower cylinder shedding in the same direction are observed in Figs. 24 and 25, this result is also consistent with the response correlation in Fig. 19(a). The in-phase pattern from the SBS configuration leads the upper and lower cylinders to vibrate in the same direction. In this case, the gap between

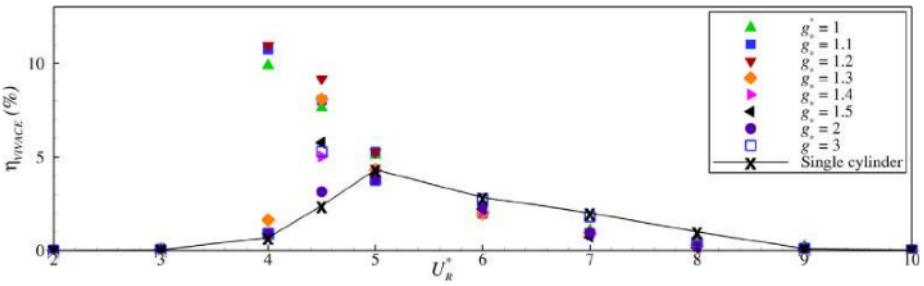

Fig. 26. The efficiencies of single cylinder and SBS cylinders with respect to U_R^*.

cylinders will remain constant while both cylinders vibrate, as shown in Figs. 24 and 25. The constant gap in the in-phase response leads to the almost constant gap flow, so there is no significant increase in lift force when an in-phase vortex-shedding pattern occurs. The following video animation will clearly show the difference between in-phase and anti-phase correlations, as well as the possibility of cylinder collision on anti-phase correlation (link to video animation: https://www.youtube.com/watch?v=oymg0y2L8GI).

6.3. Efficiency of VIVACE

Efficiency is the most important factor to consider in energy converter equipment. The quantity of energy extracted from the available potential energy is generally represented by this information. The efficiency of the vibrating cylinder with respect to reduced velocity is calculated using the efficiency formula of the VIVACE converter provided by Ding et al. (Eq. (12)) (Ding et al., 2016). Fig. 26 shows the efficiency of VIVACE for single and SBS cylinder cases with respect to U_R^*. For almost all U_R^*, the efficiency of VIVACE from SBS cylinders with $g* = 3.0$ is equal to that of the single-cylinder. As a result, at this gap ratio, the effect of an SBS configuration is minor. The increase in efficiency of SBS cylinders occurs in the interval of $4.0 \leq U_R^* \leq 5.0$. Outside this range, the efficiency of SBS cylinders is lower than that of a single cylinder. The SBS cylinders with the gap ratio $g* = 1.0$–1.2 exhibit a significant increase in efficiency for this range. Based on the Eq. (12), the efficiency is calculated from amplitude and frequency responses, so the SBS cylinders with gap ratios $g^* = 1.0$–1.2 produce a better result because those cases also show higher amplitude and frequency responses. The SBS cylinders with $g* = 1.2$ have the maximum efficiency in this range. Thus we can indicate that $g* = 1.2$ is the preferable gap ratio. The SBS cylinders with the gap ratio $g^* = 1.2$ reveal higher efficiency on the initial branch until the transition point to the upper branch. Above that transition point, the efficiency is less than that in the case of a single cylinder. In the upper branch, the smaller gap ratio reduces efficiency. The larger gap ratio leads to the same efficiency as the single cylinder. The maximum efficiency of the single-cylinder is $\eta_{VIVACE} = 4.33\%$ at $U_R^* = 5.0$. For SBS cylinders with $g^* = 1.2$, the maximum efficiency is $\eta_{VIVACE} = 10.95\%$ at $U_R^* = 4.0$. It is found that the maximum increase in VIVACE efficiency is more than twofold. When compared to the VIVACE experiments that have been conducted, these efficiencies are quite low. The maximum efficiency value and the range of optimal U_R^* were significantly influenced by Re, m^*, and ζ, according to a parameter study on the energy extraction process from VIV conducted by Barrero-Gil et al. (2012). These parameters may be varied in future investigations to enlarge the U_R^* range with significant amplitude as well as maximize the resulting efficiency. According to Figs. 18, 19, and 26, the anti-phase correlation between two SBS cylinders results in better efficiency, especially at the initial branch region. The SBS cylinders with anti-phase correlation reveal better efficiency, but this condition is also destructive if a cylinder collision occurs. The minimal gap ratio may be investigated to determine the allowable gap ratio between SBS cylinders.

7. Conclusions

The VIV simulations of two circular cylinders in a SBS configuration were performed in the interval of reduced velocity $2.0 < U_R^* < 10$ with $m^* = 10.0$, $\zeta = 0.01$ and Re = 1,000. The VIV responses were studied for a range of gap ratios $1.0 < g^* < 3.0$. Moreover, the efficiency of flow energy conversion was determined to assess this configuration for the purpose of VIVACE. Regarding the effectiveness of flow energy conversion, the optimal gap ratio for an SBS arrangement was located in the interval of $1.0 \leq g^* \leq 1.2$. A significant increase in the efficiency occurred in the initial excitation region with $4.0 \leq U_R^* \leq 5.0$. Above this range, the efficiency was less than the case of a single cylinder. The early onset of the soft lock-in was observed in the case of SBS cylinders. The anti-phase correlation led to a significant increase in the vibration response as well as better efficiency. The maximum increase in the efficiency of SBS cylinders was more than twofold. On the other hand, the optimal gap ratio decreased the efficiency for other VIV branches, especially in the higher reduced velocity. In the future, passive or active flow control may be used to enhance the VIV response and the efficiency of the SBS cylinders.

CRediT authorship contribution statement

Yosua Heru Irawan: Methodology, Software, Validation, Data curation, Writing – original draft, Visualization. **Syed Ahmad Raza:** Methodology, Software, Writing – review & editing. **Ming-Jyh Chern:** Conceptualization, Investigation, Formal analysis, Resources, Supervision, Project administration, Funding acquisition.

Declaration of competing interest

The authors declare that they have no known competing financial interests or personal relationships that could have appeared to influence the work reported in this paper.

Data availability

Data will be made available on request.

Acknowledgements

The authors express their gratitude for the financial support from the Ministry of Science and Technology, Taiwan (grant no. MOST-110-2221-E-011-067) and thanks to the National Center for High-performance Computing (NCHC), Taiwan, for providing computational and storage resources.

Appendix A. Supplementary data

Supplementary material related to this article can be found online at https://doi.org/10.1016/j.apor.2022.103392.

References

Barrero-Gil, A., Pindado, S., Avila, S., 2012. Extracting energy from Vortex-Induced Vibrations: A parametric study. Appl. Math. Model. 36 (7), 3153–3160. http://dx.doi.org/10.1016/j.apm.2011.09.085.

Bearman, P.W., 2011. Circular cylinder wakes and vortex-induced vibrations. J. Fluids Struct. 27 (5–6), 648–658. http://dx.doi.org/10.1016/j.jfluidstructs.2011.03.021.

Bernitsas, M.M., Raghavan, K., Ben-Simon, Y., Garcia, E.M., 2008. VIVACE (Vortex Induced Vibration Aquatic Clean Energy): A new concept in generation of clean and renewable energy from fluid flow. J. Offshore Mech. Arct. Eng. 130 (4), 1–15. http://dx.doi.org/10.1115/1.2957913.

Carini, M., Giannetti, F., Auteri, F., 2014. First instability and structural sensitivity of the flow past two side-by-side cylinders. J. Fluid Mech. 749 (2), 627–648. http://dx.doi.org/10.1017/jfm.2014.230.

Chang, C.C., Ajith Kumar, R., Bernitsas, M.M., 2011. VIV and galloping of single circular cylinder with surface roughness at 3.0 × 104 Re 1.2 × 105. Ocean Eng. 38 (16), 1713–1732. http://dx.doi.org/10.1016/j.oceaneng.2011.07.013.

Chen, W., Ji, C., Alam, M.M., Yan, Y., 2022a. Three-dimensional flow past two stationary side-by-side circular cylinders. Ocean Eng. 244 (December 2021), 110379. http://dx.doi.org/10.1016/j.oceaneng.2021.110379.

Chen, W., Ji, C., Xu, D., Alam, M.M., 2022b. Three-dimensional direct numerical simulations of two interfering side-by-side circular cylinders at intermediate spacing ratios. Appl. Ocean Res. 123 (April), 103162. http://dx.doi.org/10.1016/j.apor.2022.103162.

Chen, W., Ji, C., Xu, D., An, H., Zhang, Z., 2020. Flow-induced vibrations of two side-by-side circular cylinders at low Reynolds numbers. Phys. Fluids 32 (2), http://dx.doi.org/10.1063/1.5129013.

Chen, W., Ji, C., Xu, W., Liu, S., Campbell, J., 2015. Response and wake patterns of two side-by-side elastically supported circular cylinders in uniform laminar cross-flow. J. Fluids Struct. 55, 218–236. http://dx.doi.org/10.1016/j.jfluidstructs.2015.03.002.

Chern, M.J., Hsu, W.C., Horng, T.L., 2012. Numerical prediction of hydrodynamic loading on circular cylinder array in oscillatory flow using direct-forcing immersed boundary method. J. Appl. Math. 2012, http://dx.doi.org/10.1155/2012/505916.

Chern, M.J., Kuan, Y.H., Nugroho, G., Lu, G.T., Horng, T.L., 2014. Direct-forcing immersed boundary modeling of vortex-induced vibration of a circular cylinder. J. Wind Eng. Ind. Aerodyn. 134, 109–121. http://dx.doi.org/10.1016/j.jweia.2014.08.015.

Chern, M.J., Lu, G.T., Kuan, Y.H., Chakraborty, S., Nugroho, G., Liao, C.B., Horng, T.L., 2018. Numerial study of vortex-induced vibration of circular cylinder adjacent to plane boundary using direct-forcing immersed boundary method. J. Mech. 34 (2), 177–191. http://dx.doi.org/10.1017/jmech.2017.55.

Chern, M.J., Purnadiana, F.R., Noor, D.Z., Horng, T.L., Chau, S.W., Odhiambo, E., 2015. Numerical study of flow past two counter rotating cylinders using immersed boundary method. J. Mar. Sci. Technol. (Taiwan) 23 (5), 761–773. http://dx.doi.org/10.6119/JMST-015-0617-1.

Chern, M.J., Rajesh Kanna, P., Lu, Y.J., Cheng, I.C., Chang, S.C., 2010. A CFD study of the interaction of oscillatory flows with a pair of side-by-side cylinders. J. Fluids Struct. 26 (4), 626–643. http://dx.doi.org/10.1016/j.jfluidstructs.2010.03.002.

Chern, M.J., Shiu, W.C., Horng, T.L., 2013. Immersed boundary modeling for interaction of oscillatory flow with cylinder array under effects of flow direction and cylinder arrangement. J. Fluids Struct. 43, 325–346. http://dx.doi.org/10.1016/j.jfluidstructs.2013.09.022.

Ding, W., Sun, H., Xu, W., Bernitsas, M.M., 2021. Experimental and computational investigation of interactive flow induced oscillations of two tandem rough cylinders at 3 x 10^4 ≤ Re ≤ 1.2 x 10^5. Ocean Eng. 223 (January), 108641. http://dx.doi.org/10.1016/j.oceaneng.2021.108641.

Ding, L., Zhang, L., Bernitsas, M.M., Chang, C.C., 2016. Numerical simulation and experimental validation for energy harvesting of single-cylinder VIVACE converter with passive turbulence control. Renew. Energy 85, 1246–1259. http://dx.doi.org/10.1016/j.renene.2015.07.088.

Fernandes, A.C., Mirzaeisefat, S., Cascão, L.V., 2014. Fundamental behavior of Vortex Self Induced Vibration (VSIV). Appl. Ocean Res. 47, 183–191. http://dx.doi.org/10.1016/j.apor.2014.04.003.

Govardhan, R., Williamson, C.H., 2000. Modes of vortex formation and frequency response of a freely vibrating cylinder. J. Fluid Mech. 420, 85–130. http://dx.doi.org/10.1017/S0022112000001233.

Guilmineau, E., Queutey, P., 2004. Numerical simulation of vortex-induced vibration of a circular cylinder with low mass-damping in a turbulent flow. J. Fluids Struct. 19 (4), 449–466. http://dx.doi.org/10.1016/j.jfluidstructs.2004.02.004.

Huang, N.E., Shen, S.S.P., 2014. Hilbert Huang Transform and Its Applications: 2nd Edition. Vol. 16, p. 400, https://doi.org/10.1142/5862.

Jiang, Z., Li, P., Feng, L., Wang, Y., Liu, L., Guo, H., 2021. Experimental investigation on the VIV of two side-by-side risers fitted with triple helical strakes under coupled interference effect. J. Fluids Struct. 101, 103202. http://dx.doi.org/10.1016/j.jfluidstructs.2020.103202.

Khalak, A., Williamson, C.H., 1996. Dynamics of a hydroelastic cylinder with very low mass and damping. J. Fluids Struct. 10 (5), 455–472. http://dx.doi.org/10.1006/jfls.1996.0031.

Khalak, A., Williamson, C.H., 1997. Fluid forces and dynamics of a hydroelastic structure with very low mass and damping. J. Fluids Struct. 11 (8), 973–982. http://dx.doi.org/10.1006/jfls.1997.0110.

Khalak, A., Williamson, C.H., 1999. Motions, forces and mode transitions in vortex-induced vibrations at low mass-damping. J. Fluids Struct. 13 (7–8), 813–851. http://dx.doi.org/10.1006/jfls.1999.0236.

Kim, E.S., Bernitsas, M.M., 2016. Performance prediction of horizontal hydrokinetic energy converter using multiple-cylinder synergy in flow induced motion. Appl. Energy 170, 92–100. http://dx.doi.org/10.1016/j.apenergy.2016.02.116.

Kondo, N., 2014. Three-dimensional computation for flow-induced vibrations of an upstream circular cylinder in two tandem circular cylinders. Int. J. Comput. Fluid Dyn. 28 (6), 461–476. http://dx.doi.org/10.1080/10618562.2014.974577.

Lee, C.M., Paik, K.J., Kim, E.S., Lee, I., 2021. A fluid-structure interaction simulation on the wake-induced vibration of tandem cylinders with pivoted rotational motion. Phys. Fluids 33 (4), http://dx.doi.org/10.1063/5.0031606.

Li, M., Bernitsas, C.C., Guo, J., Sun, H., 2021. Synergistic flow-induced oscillation of multiple cylinders in harvesting marine hydrokinetic energy. J. Offshore Mech. Arct. Eng. 143 (3), http://dx.doi.org/10.1115/1.4048877.

Liu, B., Jaiman, R.K., 2018. Dynamics and stability of gap-flow interference in a vibrating side-by-side arrangement of two circular cylinders. J. Fluid Mech. 855, 804–838. http://dx.doi.org/10.1017/jfm.2018.651.

Lucor, D., Foo, J., Karniadakis, G.E., 2005. Vortex mode selection of a rigid cylinder subject to VIV at low mass-damping. J. Fluids Struct. 20 (4 SPEC. ISS.), 483–503. http://dx.doi.org/10.1016/j.jfluidstructs.2005.02.002.

Lv, Y., Sun, L., Bernitsas, M.M., Jiang, M., Sun, H., 2021a. Modelling of a flow-induced oscillation, two-cylinder, hydrokinetic energy converter based on experimental data. Energies 14 (4), 827. http://dx.doi.org/10.3390/en14040827.

Lv, Y., Sun, L., Bernitsas, M.M., Sun, H., 2021b. A comprehensive review of nonlinear oscillators in hydrokinetic energy harnessing using flow-induced vibrations. Renew. Sustain. Energy Rev. 150 (May), 111388. http://dx.doi.org/10.1016/j.rser.2021.111388.

Matin Nikoo, H., Bi, K., Hao, H., 2019. Three-dimensional vortex-induced vibration of a circular cylinder at subcritical Reynolds numbers with low-Re correction. Mar. Struct. 66 (November 2018), 288–306. http://dx.doi.org/10.1016/j.marstruc.2019.05.004.

Munir, A., Zhao, M., Wu, H., Lu, L., 2019. Effects of gap ratio on flow-induced vibration of two rigidly coupled side-by-side cylinders. J. Fluids Struct. 91, 102726. http://dx.doi.org/10.1016/j.jfluidstructs.2019.102726.

Navrose, Mittal, S., 2013. Free vibrations of a cylinder: 3-D computations at Re=1000. J. Fluids Struct. 41, 109–118. http://dx.doi.org/10.1016/j.jfluidstructs.2013.02.017.

Neumeister, R.F., Petry, A.P., Möller, S.V., 2021. Experimental flow-induced vibration analysis of the crossflow past a single cylinder and pairs of cylinders in tandem and side-by-side. J. Press. Vessel Technol., Trans. ASME 143 (3), http://dx.doi.org/10.1115/1.4048101.

Noor, D.Z., Chern, M.J., Horng, T.L., 2009. An immersed boundary method to solve fluid-solid interaction problems. Comput. Mech. 44 (4), 447–453. http://dx.doi.org/10.1007/s00466-009-0384-5.

Pan, Z.Y., Cui, W.C., Miao, Q.M., 2007. Numerical simulation of vortex-induced vibration of a circular cylinder at low mass-damping using RANS code. J. Fluids Struct. 23 (1), 23–37. http://dx.doi.org/10.1016/j.jfluidstructs.2006.07.007.

Pastrana, D., Cajas, J.C., Lehmkuhl, O., Rodríguez, I., Houzeaux, G., 2018. Large-eddy simulations of the vortex-induced vibration of a low mass ratio two-degree-of-freedom circular cylinder at subcritical Reynolds numbers. Comput. & Fluids 173, 118–132. http://dx.doi.org/10.1016/j.compfluid.2018.03.016.

Prasanth, T.K., Behara, S., Singh, S.P., Kumar, R., Mittal, S., 2006. Effect of blockage on vortex-induced vibrations at low Reynolds numbers. J. Fluids Struct. 22 (6–7), 865–876. http://dx.doi.org/10.1016/j.jfluidstructs.2006.04.011.

Prasanth, T.K., Premchandran, V., Mittal, S., 2011. Hysteresis in vortex-induced vibrations: critical blockage and effect of m *. J. Fluid Mech. 671, 207–225. http://dx.doi.org/10.1017/S0022112010005537.

Raghavan, K., Bernitsas, M., 2011. Experimental investigation of Reynolds number effect on vortex induced vibration of rigid circular cylinder on elastic supports. Ocean Eng. 38 (5–6), 719–731. http://dx.doi.org/10.1016/j.oceaneng.2010.09.003.

Raza, S.A., Chern, M.J., Susanto, H., Zhou, Y.H., 2020. Numerical investigation of the effects of a small fixed sphere in tandem arrangement on VIV of a sphere. J. Wind Eng. Ind. Aerodyn. 206 (September 2019), 104368. http://dx.doi.org/10.1016/j.jweia.2020.104368.

Raza, S.A., Irawan, Y.H., Chern, M.-J., 2021. Effect of boundary conditions and domain size on the turbulent flow characteristics over a circular cylinder. J. Chin. Inst. Eng. 44 (7), 659–672. http://dx.doi.org/10.1080/02533839.2021.1940295.

Sarpkaya, T., 2004. A critical review of the intrinsic nature of vortex-induced vibrations. J. Fluids Struct. 19 (4), 389–447. http://dx.doi.org/10.1016/j.jfluidstructs.2004.02.005.

Sumner, D., 2010. Two circular cylinders in cross-flow: A review. J. Fluids Struct. 26 (6), 849–899. http://dx.doi.org/10.1016/j.jfluidstructs.2010.07.001.

Sun, H., Kim, E.S., Nowakowski, G., Mauer, E., Bernitsas, M.M., 2016. Effect of mass-ratio, damping, and stiffness on optimal hydrokinetic energy conversion of a single, rough cylinder in flow induced motions. Renew. Energy 99, 936–959. http://dx.doi.org/10.1016/j.renene.2016.07.024.

Vedeld, K., Nestegård, A., 2021. Vortex induced vibrations of short side by side cylinders. Mar. Struct. 79 (July 2020), 102996. http://dx.doi.org/10.1016/j.marstruc.2021.102996.

Wang, J.-s., Fan, D., Lin, K., 2020. A review on flow-induced vibration of offshore circular cylinders. J. Hydrodyn. 32 (3), 415–440. http://dx.doi.org/10.1007/s42241-020-0032-2.

Wang, E., Xiao, Q., Incecik, A., 2017. Three-dimensional numerical simulation of two-degree-of-freedom VIV of a circular cylinder with varying natural frequency ratios at Re=500. J. Fluids Struct. 73, 162–182. http://dx.doi.org/10.1016/j.jfluidstructs.2017.06.001.

Wang, J., Zhou, S., Zhang, Z., Yurchenko, D., 2019. High-performance piezoelectric wind energy harvester with Y-shaped attachments. Energy Convers. Manage. 181 (December 2018), 645–652. http://dx.doi.org/10.1016/j.enconman.2018.12.034.

Williamson, C.H., Govardhan, R., 2004. Vortex-induced vibrations. Annu. Rev. Fluid Mech. 36 (1982), 413–455. http://dx.doi.org/10.1146/annurev.fluid.36.050802.122128.

Williamson, C.H., Govardhan, R., 2008. A brief review of recent results in vortex-induced vibrations. J. Wind Eng. Ind. Aerodyn. 96 (6–7), 713–735. http://dx.doi.org/10.1016/j.jweia.2007.06.019.

Xu, W., Wu, H., Sha, M., Wang, E., 2022. Numerical study on the flow-induced vibrations of two elastically mounted side-by-side cylinders at subcritical Reynolds numbers. Appl. Ocean Res. 124 (January), 103191. http://dx.doi.org/10.1016/j.apor.2022.103191.

Yuan, W., Sun, H., Kim, E.S., Li, H., Beltsos, N., Bernitsas, M.M., 2021. Hydrokinetic energy conversion by flow-induced oscillation of two tandem cylinders of different stiffness. J. Offshore Mech. Arct. Eng. 143 (6), 1–11. http://dx.doi.org/10.1115/1.4050641.

Zhao, M., Cheng, L., An, H., Lu, L., 2014. Three-dimensional numerical simulation of vortex-induced vibration of an elastically mounted rigid circular cylinder in steady current. J. Fluids Struct. 50, 292–311. http://dx.doi.org/10.1016/j.jfluidstructs.2014.05.016.

Zhao, M., Pearcey, T., Cheng, L., Xiang, Y., 2017. Three-dimensional numerical simulations of vortex-induced vibrations of a circular cylinder in oscillatory flow. J. Waterway, Port, Coast. Ocean Eng. 143 (4), 1–16. http://dx.doi.org/10.1061/(ASCE)WW.1943-5460.0000391.

Zhou, Y., Alam, M., 2016. Wake of two interacting circular cylinders: A review. Int. J. Heat Fluid Flow 62, 510–537. http://dx.doi.org/10.1016/j.ijheatfluidflow.2016.08.008.

Zou, Q., Ding, L., Zou, R., Kong, H., Wang, H., Zhang, L., 2021. Two-degree-of-freedom flow-induced vibration of two circular cylinders with constraint for different arrangements. Ocean Eng. 225 (January), 108806. http://dx.doi.org/10.1016/j.oceaneng.2021.108806.

Numerical predictions of vibration responses and flow energy conversion efficiency of side-by-side cylinders at moderate Reynolds number

ORIGINALITY REPORT

24%	12%	22%	3%
SIMILARITY INDEX	INTERNET SOURCES	PUBLICATIONS	STUDENT PAPERS

MATCH ALL SOURCES (ONLY SELECTED SOURCE PRINTED)

2%

★ Pandeng Yin, Jianjian Xin, Fulong Shi, Yafei Li, Xiangyu Liu, Liang Shu. "Numerical study on hydrodynamic interaction characteristics of vortex-induced vibration of two side-by-side cylinders near the wall", Ocean Engineering, 2024

Publication

Exclude quotes	Off	Exclude matches	Off
Exclude bibliography	On		